Three-dimensional flow in the subslab mantle

Karen Paczkowski[1,2], Laurent G. J. Montési[1], Maureen D. Long[2], and Christopher J. Thissen[2]

[1]Department of Geology, University of Maryland, College Park, Maryland, USA, [2]Department of Geology and Geophysics, Yale University, New Haven, Connecticut, USA

Abstract Three-dimensional models of mantle flow at subduction zones make it possible to explain the common occurrence of trench-parallel subslab seismic anisotropy. Subslab flow becomes inherently three-dimensional when slab-driven flow interacts with a wide variety of ambient background mantle flow conditions. This interaction depends on slab geometries, mechanical coupling parameters, and lower mantle viscosities. Deflection of subslab mantle flow is a robust feature for all model parameters and geometries as the slab acts as an obstruction to the ambient, background mantle flow. Background mantle flow can become trench-perpendicular or trench-parallel subslab flow depending on whether the ambient background mantle flow is deflected beneath the bottom of the slab or toward the edge of the slab. The first case is especially prominent in models with short slabs that do not penetrate into the lower mantle. The second case is especially prominent in models with long, steep slabs. The results are also highly sensitive to the amount of mechanical coupling between the subducting plate and the mantle beneath it. High levels of coupling create a boundary layer of trench-perpendicular entrained flow, pushing the deflection due to the obstructing slab away from the slab. We compare our subslab flow model predictions with a global set of seismic anisotropy fast directions in the subslab mantle, and find generally good agreement between the anisotropy observations (dominantly trench-parallel or trench-perpendicular) and the mantle flow directions predicted for decoupled systems.

1. Introduction

Two-dimensional models of mantle flow in subduction zones typically involve a subducting plate viscously coupled to the adjacent upper mantle [e.g., *Tovish et al.*, 1978; *McKenzie*, 1979; *Fischer et al.*, 2000; *Long et al.*, 2007]. In these models, the downgoing plate entrains flow in the subslab mantle, driving subslab mantle flow in the direction of subducting plate motion. The two-dimensional model of entrained mantle flow fields in the subslab region has been the standard against which seismic anisotropy observations have often been compared [*Russo and Silver*, 1994; *Long and Silver*, 2008, 2009]. However, observations suggest that this simple two-dimensional model is inadequate to explain the available data for many of the world's subduction zones. In particular, for many subduction zones, the seismically fast direction in the subslab mantle aligns roughly parallel with the trench, which is perpendicular to the direction predicted by the two-dimensional corner flow model (see recent compilations by *Long and Silver* [2008, 2009], *Long* [2013], and *Lynner and Long* [2014b].

A number of hypotheses have been developed to explain these seismic anisotropy observations, including toroidal flow induced by trench migration [*Russo and Silver*, 1994; *Long and Silver*, 2008, 2009], aligned serpentinized cracks in the shallow part of the slab [*Faccenda et al.*, 2008], pressure-induced formation of B-type olivine in the subslab mantle [*Jung et al.*, 2009], rotation of seismic anisotropy frozen in subducted oceanic asthenosphere [*Song and Kawakatsu*, 2012, 2013], and age-related decoupling of the subducting plate from the formation of a thin frozen gabbro layer [*Karato*, 2012] or the onset of small-scale convection [*Lynner and Long*, 2014b]. The possibility of three-dimensional flow in subduction systems has been explored extensively from a modeling perspective [e.g., *Buttles and Olson*, 1998; *Kincaid and Griffiths*, 2003, 2004; *Funiciello et al.*, 2003, 2004, 2006; *Schellart*, 2004; *Druken et al.*, 2011; *Faccenda and Capitanio*, 2012, 2013; *Rodríguez-González et al.*, 2014a; *Li et al.*, 2014]. Many modeling studies have focused on flow in the wedge mantle or in the vicinity of a slab edge [e.g., *Lowman et al.*, 2007; *Kneller and van Keken*, 2007, 2008; *Jadamec and Billen*, 2010; *Stadler et al.*, 2010a; *Rodríguez-González et al.*, 2014a], while fewer studies have focused on the subslab mantle. *Paczkowski et al.* [2014b] recently proposed a model to quantitatively explain the
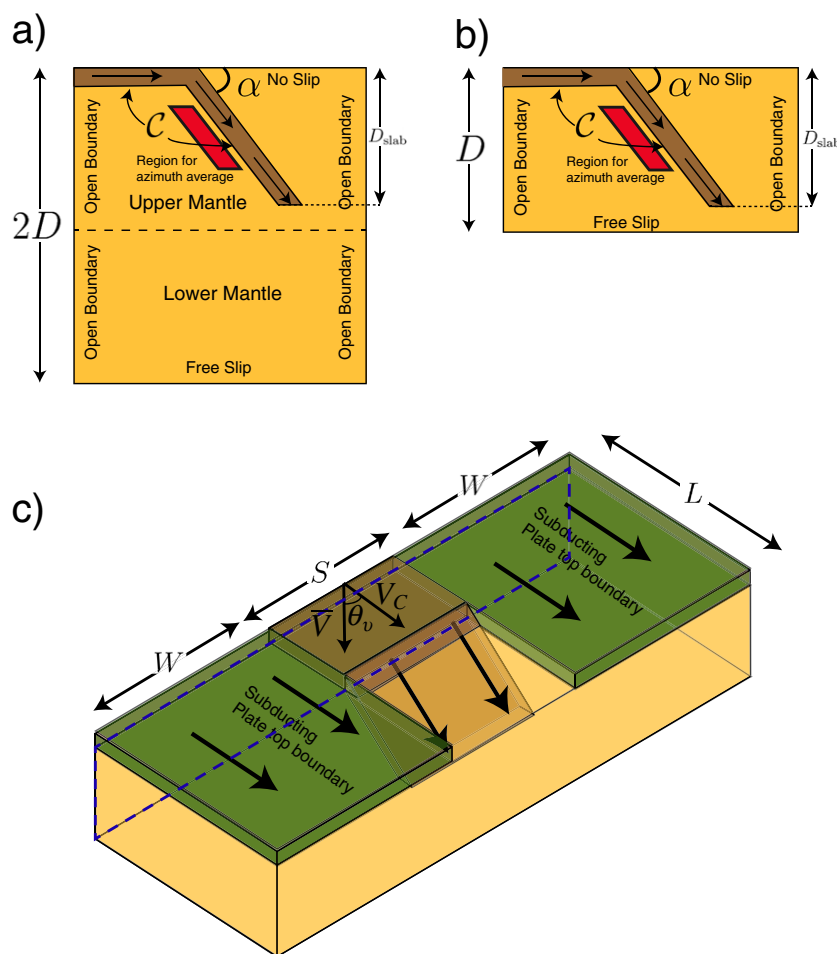
Figure 1. Schematic drawing of model setup and boundary conditions in a cross section at the midpoint of the model when a lower mantle is (a) present and (b) absent, and (c) as a three-dimensional perspective view. We consider two different top boundary conditions, where the majority of the top boundary is part of either the subducting slab or the overriding plate. When the top boundary is primarily composed of the overriding plate the green regions are solved for as part of the mantle. When the top boundary is primarily composed of the subducting plate the green regions have a set velocity V_C and the same coupling coefficient $\mathcal{C}$ as the subducting plate. The overriding plate is not shown. The convention for defining $\bar{V}$ and θ_v relative to the convergence velocity, V_C are indicated in Figure 1c. The location where $\bar{V}$ and θ_v are calculated for each model is shown by the dotted blue box in Figure 1c.

seismic anisotropy directions from a uniform database of subslab shear wave splitting measurements for about a dozen subduction zones [*Lynner and Long*, 2014bb] by modeling a background mantle flow field deflected by subducting slabs.

Here we expand on that work by developing a new geodynamic framework against which subslab seismic anisotropy directions can be evaluated. We discuss the flow directions expected in a subslab mantle domain for a wide variety of subduction zone geometries and model parameters. We investigate the sensitivity of the flow fields to boundary conditions, such as degree of coupling between the slab and the subslab mantle, slab geometry, slab kinematics, lower mantle viscosity, trench migration, and background mantle flow. In these models, the slab acts as an obstruction, deflecting the background mantle flow field either beneath the slab (creating trench-perpendicular subslab flow), or around the slab (creating trench-parallel subslab flow). Whether the subslab mantle flow is dominantly trench-parallel or trench-perpendicular depends heavily on the background mantle flow direction and intensity, subslab decoupling, and slab geometry. The general trends observed in these models can be used as an improved standard to the two-dimensional corner flow entrained models to guide the interpretation of seismic anisotropy in the subslab mantle and identify which subduction zones exhibit truly anomalous seismic anisotropy behavior.

In our previous work, we restricted our quantitative comparison between seismic anisotropy observations and our subduction zone geodynamic model results to a specific, high quality database of source-side

Table 1. Geometrical Parameters Used in the Numerical Models, as Shown in Figure 1

Parameter	Value (D)	Value (km)
D	1	670
L	$\cot\alpha + 2.2$	$670\cot\alpha + 1474$
W	2.5	1675
S	1.5	1005

splitting measurements [*Lynner and Long*, 2014bb]. Here we expand on those results, using the full database of available seismic anisotropy directions [*Long and Silver*, 2008, 2009]. Recognizing that splitting in the mantle wedge complicates subslab anisotropy observations for many subduction zones [e.g., *Long and Wirth*, 2013], we make a simplified characterization of each subduction zone segment as having either roughly trench-parallel or trench-perpendicular seismic anisotropy directions and compare this broad characterization with the average subslab flow direction predicted by our subduction zone models. We find that our models successfully predict the first-order subslab seismic anisotropy geometry in nearly all subduction zones worldwide.

2. Model Setup

We construct a slab-driven numerical model of mantle flow (Figure 1) using COMSOL Multiphysics®, which has been shown to have excellent performance for subduction zone modeling [*van Keken et al.*, 2008]. COMSOL Multiphysics® 4.3 is a finite element analysis solver that uses P2-P1 elements for fluid dynamics calculations. Mass and momentum conservation, given as

$$\nabla \cdot \vec{v} = 0 \tag{1}$$

and

$$-\mu\nabla^2\vec{v} + \rho\left(\vec{v}\cdot\nabla\right)\vec{v} + \nabla p = 0, \tag{2}$$

are solved for incompressible, constant viscosity, laminar flow, where μ is the viscosity, $\vec{v}$ is the velocity, and p is the pressure. The density is set to the low value of 10^{-20} kg/m³ to minimize the effects of inertia. The effects of thermal buoyancy and rheological nonlinearity and heterogeneities are ignored in these simple models. Future work should evaluate the effects of these complexities on our results.

Model geometry is symmetric with a straight trench of length S centered in the model box of length L, depth D, and width $S+2W$, where W is the width of a buffer zone on the side of the slab (Figure 1 and Table 1). The geometrical parameters, L, W, and S are chosen to minimize the boundary effects in the region of interest. The model extends to a depth $D = 670$ km or $D = 1340$ km when we include the lower mantle. We impose the geometry of the slab, with a constant dip angle, α, and maximum slab depth, D_{slab}, for each model case. The subducting plate is approximately 100 km thick. We solve for the instantaneous mantle flow only in the region surrounding the plates. In most models, the top boundary is comprised primarily of the subducting plate, where the green regions in Figure 1 are set at the subducting velocity. For models where the top boundary is comprised primarily by the overriding plate, these green regions are solved for as part of the mantle. The average flow directions in the subslab mantle tend be similar for both top boundary cases (supporting information), and we focus here only on cases where the top boundary is composed of mostly the subducting plate. A summary of the model dimensions is given in Table 1.

The wedge and subslab domains are meshed with high-resolution tetrahedrals with a range in sizes from 0.05 D to 0.1 D. The surrounding mantle edges are meshed to match the subslab and wedge resolution at the slab edge and then decay to a lower resolution away from the slab (Figure 2). All the elements are quadratic, producing solutions with higher degrees of freedom than linear elements, allowing us to use half of the nodes required for a linear element model while still obtaining a higher numerical accuracy. We verify that the model resolution is sufficient by comparing the solutions presented here with a few higher resolution models.

2.1. Background Mantle Flow, Trench Reference Frame

A background mantle flow is induced by imposing on the vertical walls of the model an external pressure field that varies linearly with the map view coordinates, x, and, y. The external pressure field is parameterized by a pressure drop per unit length, ΔP, and the angle, positive clockwise, between the pressure gradient and the subduction direction.

When a lower mantle is included, the sides of the lower mantle are open boundaries. The model results do not change significantly when the pressure gradient is also applied across the lower mantle (supporting information).
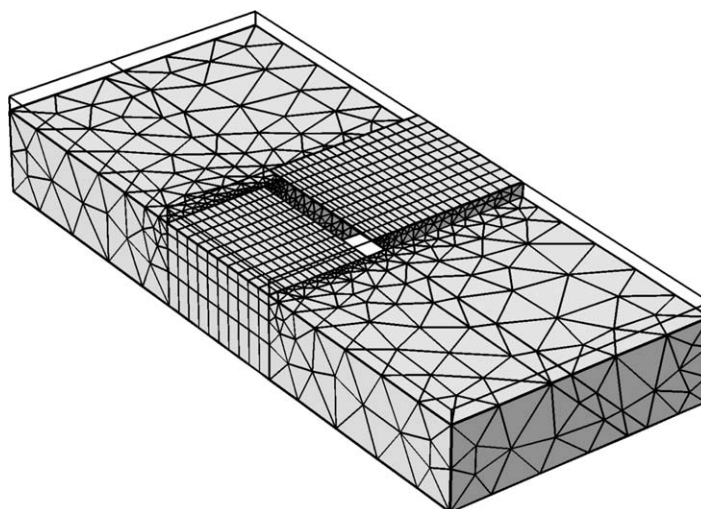
Figure 2. Mesh used for the three-dimensional model. A high resolution mesh is used in the wedge and subslab domains, while the mesh resolution decays to lower values toward the edge of the model. All elements are quadratic, allowing for twice the resolution visualized here. When a lower mantle is present it is meshed using the lower resolution mesh.

The intensity and direction of the pressure gradient are varied systematically to produce a wide range of background mantle flow configurations. The background velocity field intensity and azimuth, $\bar{V}$ and θ_v, are defined in the reference frame of a fixed trench. The velocity $\bar{V}$ is scaled by the convergence velocity of the plates at the surface, V_c. Conceptually, the background velocity field is the combination of two processes: trench migration and global mantle flow. In our calculations, only the combined effect of these processes is important as it is represented only as a large-scale pressure gradient. However, for comparison with observation, it is important to evaluate the background mantle flow at specific subduction zones. As our simulations are conducted in the reference frame fixed with the trench, trench migration appears as a translational component of the background mantle flow rather than a motion of the trench in a reference frame fixed with the mantle. Global mantle flow is driven by plate motions and density anomalies [e.g., *Conrad and Behn*, 2010] and can also be expressed in a trench-fixed reference frame (see section 4). In our models, the background mantle velocity results from the imposed pressure gradient. It is computed from the flow solution by averaging the velocity on the back face of the model (Figure 1c). The background velocity is not sensitive to the averaging location. The back side of the model was selected for consistency when comparing with the models we use to estimate the background mantle flow at actual subduction zones (section 4).

2.2. Quantifying Average Subslab Flow Directions, ϕ

To quantify the prevailing direction of the subslab flow, we calculate the average, ϕ, of the absolute value of the angle of the flow field, ϕ' in an averaging region (red box in Figures 1a and 1b) that roughly corresponds to the region sampled by shear wave splitting data in the subslab mantle [e.g., *Foley and Long*, 2011]. The region includes material approximately 200 km from the slab, extends to the base of the upper mantle, and includes points close to the slab while avoiding numerical noise at the model boundary and any artificially induced shear gradients at the edges of the slab. Specifically, the region extends from approximately 160 to 435 km depth, approximately 200 to 67 km behind the slab, and 670 km along the strike of the slab. Our average subslab velocity angle results do not depend heavily on the size of this averaging region.

2.3. Boundary Conditions

Our model has a free-slip bottom in addition to the pressure boundary conditions on the vertical sides that are described in section 2.1. The model results do not change significantly for a no-slip bottom boundary condition.

The top surface of the mantle connected to the overriding plate is fixed with a no-slip boundary condition. This defines the reference frame of the model to be fixed with the trench, defined as the edge of a nondeforming, overriding plate [*Morgan*, 1968].

The subducting plate is moving at the convergence velocity, V_c. In our model, all the velocity components are normalized to V_c. Therefore, the tangential velocity of the subducting plate and the downgoing slab are 1. Coupling to the flow along the slab-wedge interface is defined by a smoothed Heaviside function with a continuous second derivative that transitions the mantle wedge from fully decoupled at depths shallower than 80 km to fully coupled at a depth deeper than 80 km [*Wada and Wang*, 2009].
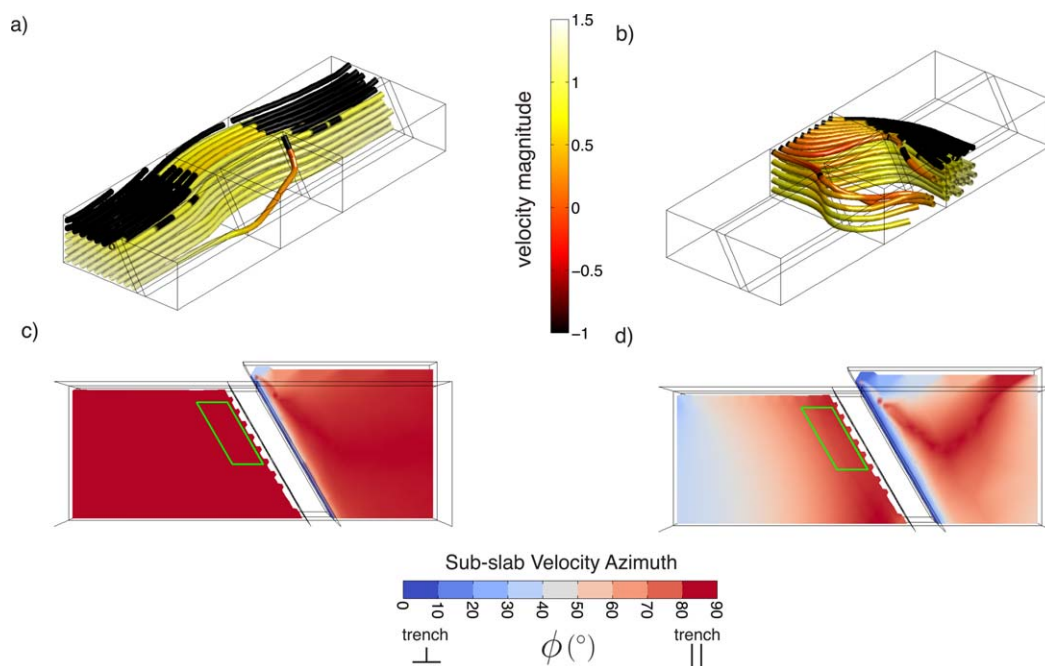
Figure 3. (a and b) Subslab mantle streamlines and (c and d) flow azimuth, ϕ', in a cross section at the midpoint of the model using the "reference case" geometry. The model presented here features a background mantle flow with velocity $\bar{V}=1$ and either a trench-parallel ($\theta_v=90°$, left column) or nearly trench-perpendicular ($\theta_v=-11°$, right column) flow azimuth.

The mantle below the slab is mechanically coupled to the subducting plate using a velocity boundary condition consistent with the rigid slab in the model. The mantle velocity along the base of the slab is obtained by multiplying the slab velocity by a coupling factor $\mathcal{C}$. A fully coupled system corresponds to $\mathcal{C}=1$, while a fully decoupled system corresponds to $\mathcal{C}=0$. The coupling factor is constant along the entire interface between the subslab mantle and the subducting plate, including the back of the slab. The sides and bottom of the subducting slab are fully coupled to the surrounding mantle for all models.

3. Model Results

3.1. Subslab Flow Field for a "Reference Case" Without Coupling Along the Base of the Slab

To introduce the main concepts and explain the resulting azimuth directions, we first present a "reference case" model run (Figure 3). This model approximates the slab morphology of northern Tonga, with a slab dip of $\alpha=60°$, a slab length of $D_{slab}=670$ km, and a top boundary primarily under the subducting plate. We start with no lower mantle and a fully decoupled interface between the slab and the subslab mantle ($\mathcal{C}=0$). We run two end-member cases of background mantle flow ($\theta_v=90°$ and $\theta_v=-11°$), where the latter case closely resembles the trench-perpendicular background mantle flow velocity in the trench-fixed reference frame resulting from rapid rollback for northern Tonga [*Schellart et al.*, 2008]. In both cases, the magnitude of the background flow is $\log_{10}(\bar{V})=1$.

For the case of trench-parallel background flow ($\theta_v=90°$), the lack of coupling between the slab and the subslab mantle combined with the strong background mantle flow allows the background mantle flow to continue undisturbed beneath the slab, with trench-parallel streamlines throughout the subslab mantle (Figure 3a). We calculate the absolute value of the flow angle, ϕ', where $\phi'=0°$ indicates trench-perpendicular flow and $\phi'=90°$ indicates trench-parallel flow at each point in the model. A cross-sectional slice through the center of the model is shown in Figure 3c, where the red colors indicate trench-parallel flow throughout the subslab mantle.

For the case of nearly trench-perpendicular background mantle flow ($\theta_v=-11°$), the flow is deflected by the slab, which acts as an obstruction (Figure 3a). The streamlines in the subslab region enter from the back of the model and are deflected along the back of the slab in a trench-parallel direction, so that mantle flows toward the slab edges. A cross-sectional slice of the velocity angle, ϕ' (Figure 3d), shows the flow in the
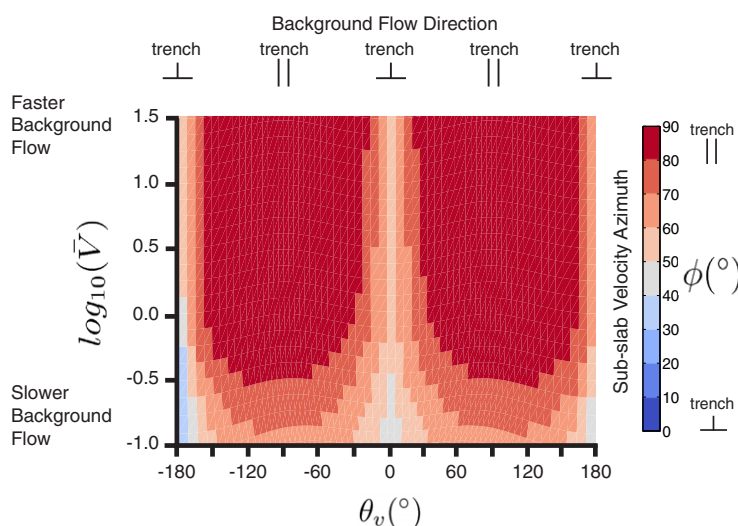
Figure 4. Average subslab flow azimuth, ϕ, as a function of the background mantle flow magnitude, $\bar{V}$, and angle θ_v, for the "reference case" model. This model has a slab geometry defined by, $\alpha=60°$, $D_{slab} = 670$, C$=0$, with a top boundary condition comprised mostly of the subducting plate, and does not include a lower mantle. Figure 4 and similar figures are contours from a suite of approximately 3000 model runs.

trench-perpendicular direction at the back of the model with a region of trench-parallel flow created directly beneath the slab.

The "reference case" model of Figure 3 shows that both trench-parallel and trench-perpendicular background mantle flow directions can produce trench-parallel mantle flow immediately below the slab for a fully decoupled system ($\mathcal{C}=0$) with a slab that extends to the base of the transition zone with a relatively steep dip ($\alpha=60°$).

3.2. Effects of Background Mantle Flow Intensity and Direction

To further understand the influence of the background mantle velocity field (including the effects of trench migration) on subslab flow, we start with our "reference case" model, and vary the magnitude and the angle of the pressure gradient sufficiently to include the full range of background velocities typical of mantle flow [e.g., *Conrad and Behn*, 2010]. We calculate the average flow direction, ϕ, in the subslab sample box for each case and plot our results as a function of the background mantle flow characteristics (Figure 4). The stepsize for the variations in pressure gradient and orientation is chosen so that Figure 4 and similar figures are contoured from approximately 3000 model runs (approximately 5° steps in orientation and 46 steps in magnitude). The smoothness of the fields suggests that this resolution is sufficient to resolve the gradients on the average flow direction.

The model results for the "reference case" geometry are dominated by trench-parallel subslab flow for most background mantle flow fields. For weak background mantle flow $\left(\bar{V} \leq \approx \frac{1}{3}\right)$, the average subslab flow direction, ϕ, is primarily dependent on θ_v and is only weakly dependent on $\bar{V}$. When the background mantle flow is trench-perpendicular and $\bar{V}$ is relatively high, the resulting average subslab flow field direction is $\phi \approx 50°-60°$ regardless of background flow direction. However, when the background mantle flow is trench-parallel, the resulting subslab flow direction is $\phi \approx 90°$.

3.3. Effects of Coupling Between the Slab and the Subslab Mantle

Using our "reference case" model, we vary the amount of coupling between the subducting plate and the subslab mantle, $0 \leq \mathcal{C} \leq 1$. In the coupled models, the slab entrains a boundary layer of flow in a trench-perpendicular direction (Figures 5a and 5b). The thickness of this entrained layer increases with the coupling factor. Trench-parallel background flow continues through most of the subslab region, and trench-perpendicular background flow is still deflected around the slab edges but the deflection happens further back from the slab, behind the boundary layer of slab-entrained flow.

The relative importance of slab-entrained flow and the background flow in the subslab sampling box in fully coupled and partially coupled systems depends on $\bar{V}$, as seen by comparing the average subslab flow azimuth, ϕ, for various values of $\mathcal{C}$ (Figures 6a–6d). The coupling factor and background flow velocity have competing effects on the thickness of slab-entrained mantle, which may or may not overlap the subslab region where we sample mantle flow azimuth. A fully coupled system requires larger values of $\bar{V}$ than for the fully decoupled system to systematically produce trench-parallel flow fields in the subslab mantle. The
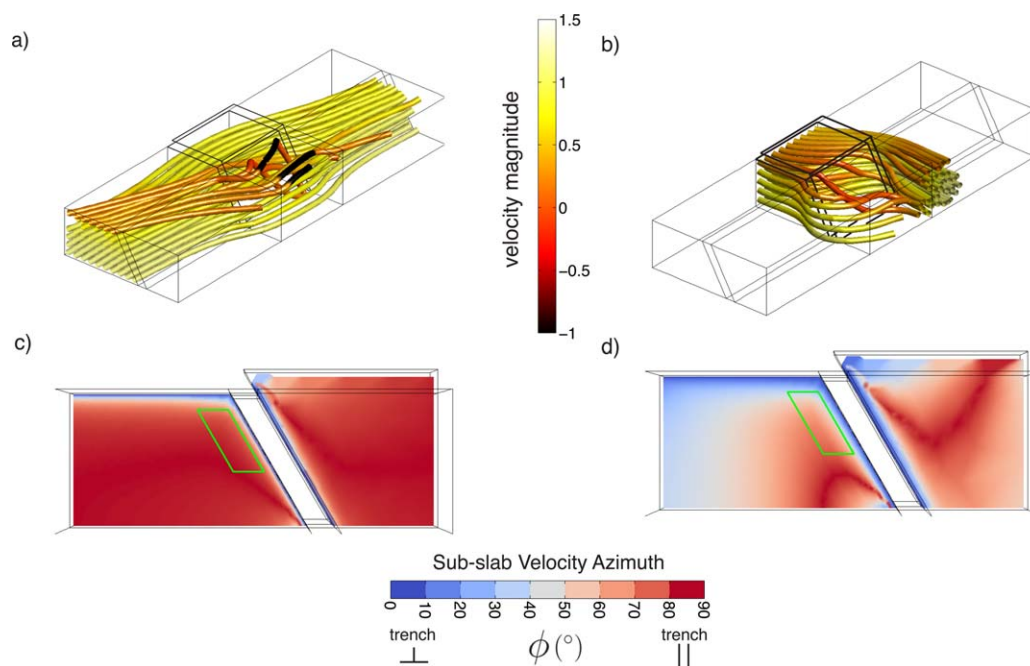
Figure 5. (a and b) Subslab mantle streamlines and (c and d) flow azimuth, ϕ', in a cross section at the midpoint of the model for the "reference case" model as in Figure 3 but with full coupling ($\mathcal{C}=1$). The left column shows the results for trench-parallel background mantle flow and the right column shows the results for trench-perpendicular background mantle flow $\bar{V}=1$ in both models.

magnitude of $\bar{V}$ necessary for the three-dimensional component of flow to overcome the entrained flow increases with the coupling factor. In general, models with $\mathcal{C} \leq 0.01$ closely resemble the fully decoupled model and models with $\mathcal{C} \geq 0.75$ closely resemble the fully coupled model.

3.4. Effects of Slab Geometry

We also test the sensitivity of subslab flow field to slab geometry by varying the slab dip angle, $15° \leq \alpha \leq 90°$ and the slab depth, 335 km $\leq D_{slab} \leq 670$ km from our "reference case" model.

Slabs that dip steeply ($\alpha \geq 60°$) generate significant trench-parallel flow for all background mantle flow field combinations (Figures 6f, 8b, and 8c). The resulting flow in the subslab is highly trench-parallel, with values close to $\phi=90°$ for even lower values of $\bar{V}$ than for the "reference case" ($\bar{V} < 0.1$). In contrast, for a shallowly dipping slab ($\alpha \leq 30°$) subslab flow follows the azimuth of the background flow field even when the background velocity is much higher than the convergence velocity ($\bar{V} > 1$, Figure 6e). It is clear that the dip of the slab exerts a major control on how strong an obstruction the slab is and therefore how much flow redirection is needed for the mantle to flow toward the slab edges.

We also examine cases with shorter slab penetration depths. As with deep slabs, trench-parallel background mantle flow fields tend to produce trench-parallel subslab flow. Trench-perpendicular background mantle flow, however, is deflected beneath the slab creating trench-perpendicular subslab flow, even with steeply dipping slabs (Figures 7a, 7c, 8d, and 8e). The reorientation does not require a change in flow azimuth, and therefore, the background mantle flow field direction is preserved in the subslab domain, especially if the background flow velocity, $\bar{V}$, is high (Figures 7a, 7c, 8d, and 8e). This contrasts with the behavior for deep slabs, in which flow is reoriented along strike.

For cases in which the mantle flow is deflected beneath the slab, other scenarios for seismic anisotropy symmetry may predict a fast splitting direction at a right angle from the flow direction. For example, if the dip of the LPO fast symmetry axis exceeds $\sim70°$ [*Skemer et al.*, 2012] or if the elastic tensor suggested by *Song and Kawakatsu* [2012, 2013] attains a dip of $\sim65°$ (depending on the subduction obliquity and the back azimuth and incidence angle of the seismic wave), then trench-parallel fast splitting directions would be expected if mantle flow is trench-perpendicular. In our models, however, the average vertical angle of the flow direction in all cases is less than $65°$.
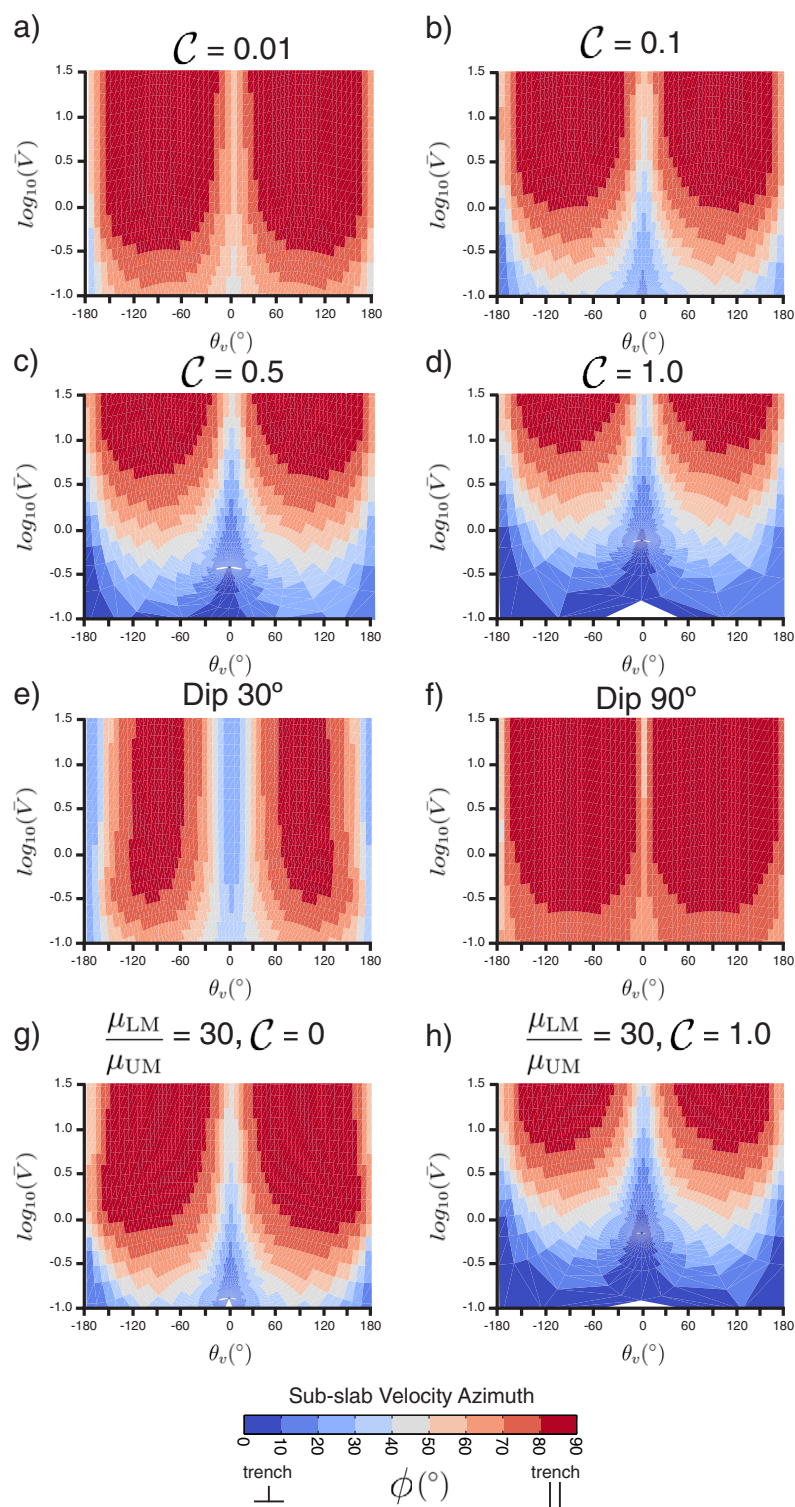
Figure 6. (a–d) Same as Figure 4 for variations on the "reference case" model with increased coupling $\mathcal{C}$, (e and f) modified slab dip, and (g and h) including a lower mantle.

3.5. Effects of Lower Mantle Viscosity

The model configuration with no lower mantle is a good approximation for cases in which the slab does not extend all the way to the bottom of the model and for the cases where the 670 km discontinuity acts as an effective barrier to flow and the slabs themselves are deflected, anchored, or

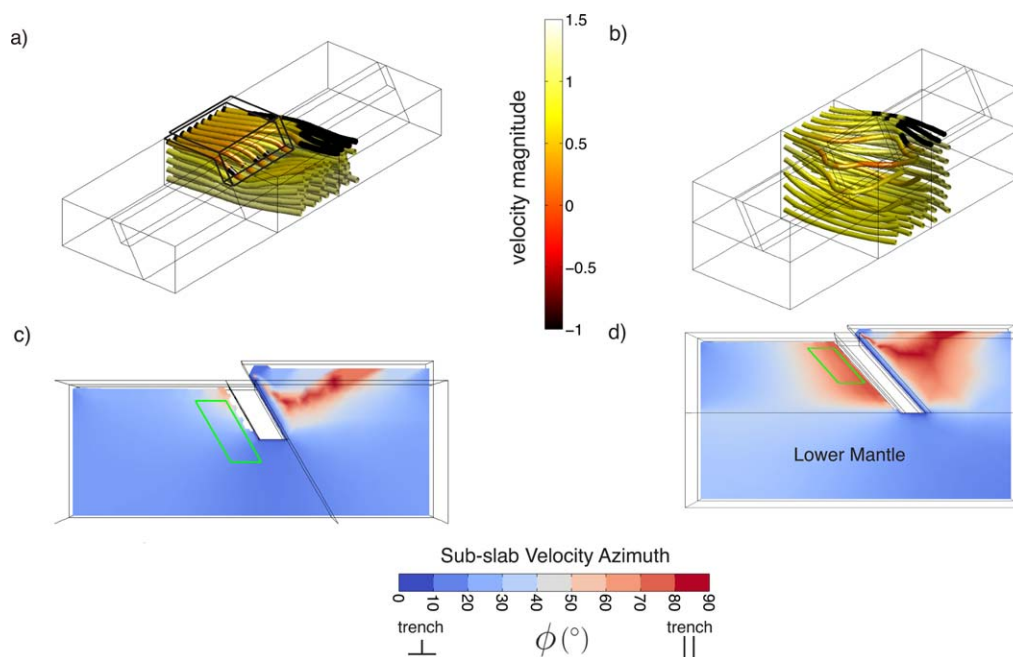**Figure 7.** (a and b) Subslab mantle streamlines and (c and d) flow azimuth ϕ' in a cross section at the midpoint of the model for simulations with trench-perpendicular mantle flow with $\bar{V}=1$ and variations on the "reference case" model with short slabs ($0.5D_{slab}$, left column) or a high viscosity lower mantle $\left(\frac{\mu_{LM}}{\mu_{UM}}=30,\text{rightcolumn}\right)$.

stagnate at the 670 km transition; in such cases there is an effective barrier to entrained flow at the 670 km discontinuity. Specifically, when the slab does not penetrate into the lower mantle due to viscosity increases, it is reasonable that entrained flow of the less viscous surrounding mantle will be deflected as well. Additionally, when a slab extends far into the deep lower mantle, the slab presumably acts as a deep barrier to flow at depth, preventing mantle from escaping beneath the slab. However, it is possible that in a general case, background mantle flow may in fact be deflected downward beneath deep slabs through the lower mantle. In this case, flow geometries similar to our short slab models, without significant azimuth flow adjustment, are to be expected. To test this scenario, we expand our "reference case" model to $D = 1340$ km and vary the ratio of lower mantle viscosity to the upper mantle viscosity, $1 \leq \frac{\mu_{LM}}{\mu_{UM}} \leq 1000$. The lower mantle has a free-slip bottom and open sides without an imposed pressure gradient.

We find that for models that include a lower mantle and slab reaching the base of the upper mantle, the subslab flow field still encompasses a robust component of trench-parallel flow (Figures 6g and 6h) even if the lower mantle viscosity is only 30 times that of the upper mantle, and when the slab is fully coupled (Figures 7b and 7d). The flow toward the slab in the upper mantle is still largely deflected around the slab in the trench-parallel direction, while only streamlines near the 670 km boundary are deflected beneath the slab. Streamlines that originate within the lower mantle continue beneath the slab relatively undisturbed. Background mantle flow fields with lower velocity magnitudes produce subslab flow that has a weaker trench-parallel component. The addition of the lower mantle makes this trend more pronounced, requiring a higher $\bar{V}$ to produce trench-perpendicular background mantle flow fields. Trench-perpendicular background flow remains trench-perpendicular in the subslab sampling box to a larger extent in models with a lower mantle than in models without because the base of the upper mantle no longer acts as a major obstruction to downward flow.

For model cases that include a lower mantle and variable amounts of subslab coupling, we find that there is a boundary layer of slab-entrained flow beneath the subducting plate whose thickness increases with the coupling parameter $\mathcal{C}$. As in the model cases with no lower mantle, the character of the subslab flow field becomes sensitive to $\bar{V}$. These trends are robust for all viscosity ratios, and the average azimuth is not sensitive to the lower mantle viscosity.
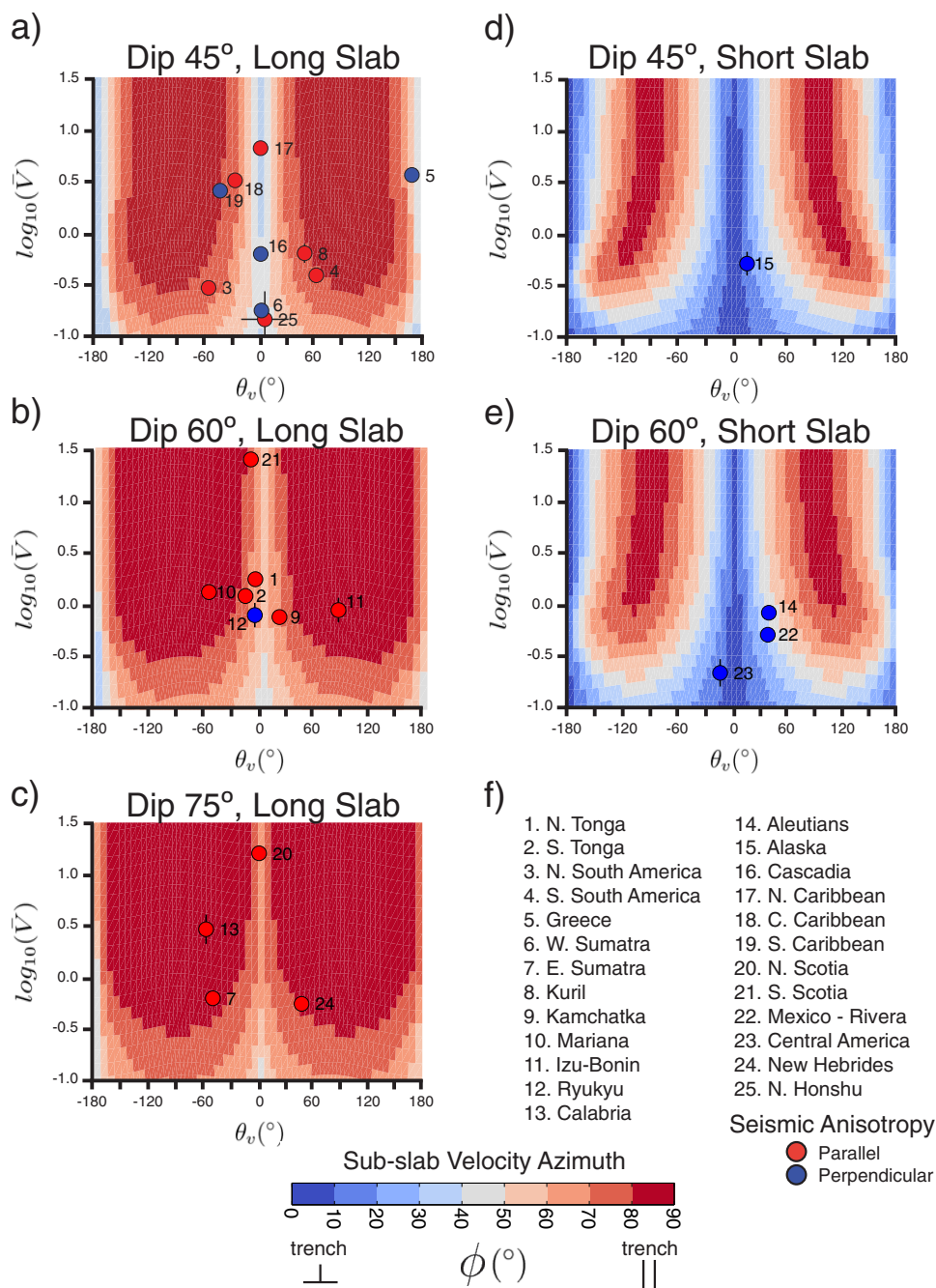
Figure 8. Comparison of observed seismic anisotropy directions with the subslab flow azimuth obtained in fully decoupled models without a lower mantle. Subduction zones are grouped by geometry and numbered. Panels a-e are similar to Figure 4, but with the geometry of each of the five slab categories as indicated in the panel title. The color of the corresponding circle indicates whether seismic anisotropy directions for that subduction zone are broadly trench-parallel or trench-perpendicular. Error bars are the same as in Table 2. The subduction zone segments that correspond to each number are given in panel f.

4. Subslab Seismic Anisotropy

4.1. Mineral Physics Considerations

It is not possible to make direct observations of the mantle flow field. Seismic anisotropy data, however, provide a reasonably direct observation of present-day mantle flow [e.g., *Long*, 2013, and references therein]. Briefly, deformation accommodated by dislocation creep in the upper mantle results in the development of lattice preferred orientation (LPO), primarily in olivine [*Ribe*, 1989, 1992; *Tommasi et al.*, 2000;

Karato et al., 2008]. In sufficiently deformed samples, the orientations of the olivine crystals become statistically aligned, resulting in macroscale anisotropy. The seismic wave speed of the macroscale material then varies with orientation, with the fast direction subparallel to the elastically fast direction of the aligned olivine crystals. Propagation of seismic waves through this coherently anisotropic material results in a directional dependence of the wave speed, called seismic anisotropy [*Mainprice*, 2007]. Shear wave splitting is a common method to measure seismic anisotropy [e.g., *Savage*, 1999; *Long*, 2013, and references therein], characterized by the delay time and the orientation of the seismically fastest wave direction.

Comparisons with observed delay times require integrated fabric development and propagation of synthetic seismic waves [e.g., *Fischer et al.*, 2000; *Long et al.*, 2007] and rely on a series of assumptions about fabric strength. In a companion paper [*Paczkowski et al.*, 2014], we carry out more detailed comparisons between the finite strain orientations predicted by our models and the flow direction. We find them to be essentially equivalent. Therefore, here, we compare seismic anisotropy with the flow directions, which are much less costly to compute. The relationship between the flow fields and seismic anisotropy directions depends heavily on the nature of LPO fabric development in olivine. Five olivine fabric types (A, B, C, D, and E-type) have been identified through experiments and petrographic examination of mantle rocks [e.g., *Jung and Karato*, 2001; *Katayama et al.*, 2004; *Jung et al.*, 2006; *Katayama and Karato*, 2006]. For A, C, D, and E fabric types under horizontal simple shear, in the absence of prior fabrics [e.g., *Skemer et al.*, 2012], with sufficiently low grain orientation lag parameters [*Kaminski et al.*, 2004], and vertically pro pagating shear waves, the LPO fast direction aligns with the shear direction and the velocity flow direction. For B-type fabric, the fast splitting direction is offset by 90° from the shear direction and velocity flow direction. The possible existence of B-type olivine in the upper mantle has been discussed extensively [e.g., *Becker*, 2008; *Jung et al.*, 2009; *Kreemer*, 2009; *Long and Silver*, 2009; *Conrad and Behn*, 2010; *Long and Becker*, 2010; *Long*, 2013], and is generally thought to be present only in small regions within the mantle wedge [e.g., *Kneller et al.*, 2005, 2008]. Here we assume a simplified relationship in which fast splitting directions roughly correspond to the direction of horizontal mantle flow [e.g., *Long and Becker*, 2010]. While this is a highly simplified assumption, it does allow us to test whether trench-parallel fast splitting directions beneath slabs may be associated with subduction systems with a strong component of predicted trench-parallel subslab flow.

4.2. Compilation of Subslab Fast Splitting Directions

To compare the seismic anisotropy data with the numerical velocity fields, we consider a data set of subslab anisotropy directions that covers 25 total subduction segments worldwide, using previously published data compiled by *Long and Silver* [2009], *Long* [2013], and *Lynner and Long* [2014bb] (Table 2). The splitting directions are partially based on SKS splitting measurements made at stations located close to the trench, which have long path lengths in the subslab mantle. SKS splitting measurements have been corrected for the effect of wedge splitting and the remaining signal reflects the subwedge contribution, which is likely mostly due to subslab anisotropy [*Long and Silver*, 2009]. For each subduction zone segment, we calculated simple circular averages of the fast directions and classified them as either generally trench-parallel if the directions were less than 45° from the local trench strike, or generally trench-perpendicular if they were more than 45° from the local trench strike, Table 2). This simplified classification obscures many important details about spatial variations in splitting [*Long and Silver*, 2008, 2009; *Long and Wirth*, 2013; *Long*, 2013; *Lynner and Long*, 2014b], but is justified in light of the many simplifications in our geodynamic models.

4.3. Slab Geometry and Background Flow Estimation

The dips of subducting slabs in the upper mantle, α, are taken from the global compilation of *Lallemand et al.* [2005] with a few exceptions: Mexico-Rivera [*Jarrard*, 1986], Greece [*Suckale et al.*, 2009], Calabria [*Baccheschi et al.*, 2011], and Mariana, N. Scotia, and N. and C. Caribbean [*Syracuse and Abers*, 2006].

Depths of slab penetration into the mantle D_{max} are taken from the same compilation [*Lallemand et al.*, 2005], except for Greece, Calabria, and Cascadia. All of these estimates are derived from global mantle tomography models and necessarily involve a degree of subjectivity. For Cascadia, *Bostock and Vandecar* [1995] and *Lallemand et al.* [2005] propose a short slab with a maximum penetration depth of 300 km, while other authors have argued for a deep slab that penetrates into the lower mantle but may be fragmented in the transition zone [*Sigloch et al.*, 2008; *Roth et al.*, 2008; *Sigloch*, 2011; *James et al.*, 2011] or the upper mantle [*Schmandt and Humphreys*, 2010; *Obrebski et al.*, 2011]. Our models do not consider the complex case of a fragmented slab. However, it may be expected that a fragmented slab would allow mantle flow beneath

Table 2. Background Mantle Flow Parameters $\bar{V}$ and θ_v [Conrad and Behn, 2010] for Each Subduction Zone in the Trench-Fixed Reference Frame[a]

	Subduction Zone	$\bar{V}$	θ_v	α_s	D_{max}(km)	ϕ_s, Reference
1	S. Scotia	24.42 ± 1.20	−11.35° ± 00.46°	65°	670	∥, *Müller et al.* [2008] and *Lynner and Long* [2013]
2	N. Scotia	16.00 ± 0.10	0.91° ± 00.51°	72°	670	∥, *Müller et al.* [2008] and *Lynner and Long* [2013]
3	N. Caribbean	6.55 ± 0.87	2.94° ± 02.05°	49°	670	∥, *Lynner and Long* [2013]
4	C. Caribbean	3.21 ± 0.13	−25.19° ± 00.39°	51°	670	∥, *Lynner and Long* [2013]
5	Calabria	2.96 ± 0.96	−57.30° ± 05.57°	70°	670	∥, *Baccheschi et al.* [2008]
6	N. Tonga	1.76 ± 0.06	−6.54° ± 01.25°	56°	670	∥, *Foley and Long* [2011]
7	Mariana	1.32 ± 0.13	−56.80° ± 02.05°	60°	900	∥, *Wookey et al.* [2005] and *Lynner and Long* [2014a]
8	S. Tonga	1.22 ± 0.04	−17.24° ± 01.33°	56°	670	∥, *Long and Silver* [2008]
9	Izu-Bonin	0.89 ± 0.24	83.55° ± 05.98°	65°	670	∥, *Hanna et al.* [2009]
10	Kamchatka	0.76 ± 0.03	19.64° ± 00.19°	56°	400–670	∥, *Peyton et al.* [2001]
11	E. Sumatra	0.64 ± 0.06	−49.86° ± 01.69°	68°	1200	∥, *Hammond et al.* [2010] and *Lynner and Long* [2014a]
12	Kuril	0.63 ± 0.13	51.58° ± 02.42°	40°	670	∥, *Lynner and Long* [2014a]
13	New Hebrides	0.56 ± 0.03	47.33° ± 01.57°	68°	670	∥, *Király et al.* [2012]
14	S. South America	0.39 ± 0.05	64.37° ± 02.34°	50°	800–1100	∥, *Anderson et al.* [2004]
15	N. South America	0.29 ± 0.03	−54.43° ± 01.12°	50°	1200	∥, *Russo and Silver* [1994]
16	N. Honshu	0.15 ± 0.09	7.68° ± 26.13°	30°	670	∥, *Lynner and Long* [2014a]
17	Aleutians	0.84 ± 0.05	40.71° ± 00.36°	60°	300–550	⊥, *Lynner and Long* [2014a]
18	Mexico-Rivera	0.51 ± 0.06	39.52° ± 03.58°	53°	300	⊥, *León Soto et al.* [2009] and *Lynner and Long* [2014a]
19	Alaska	0.49 ± 0.13	16.64° ± 03.08°	40°	300	⊥, *Hanna and Long* [2012] and *Lynner and Long* [2014a]
20	Central America	0.22 ± 0.07	−12.68° ± 06.86°	60°	400	⊥, *Lynner and Long* [2014a]
21	Greece	3.62 ± 0.07	170.11° ± 01.83°	45°	670	⊥, *Olive et al.* [2014]
22	S. Caribbean	2.55 ± 0.21	−41.67° ± 00.87°	42°	670	⊥, *Lynner and Long* [2014a]
23	Ryukyu	0.80 ± 0.21	−7.12° ± 05.18°	60°	300–670	⊥, *Lynner and Long* [2014a]
24	Cascadia	0.62 ± 0.09	3.16° ± 01.90°	45°	1200	⊥, *Russo* [2009] and *Eakin et al.* [2010]
25	W. Sumatra	0.18 ± 0.03	3.92° ± 01.63	45°	1200	⊥, *Lynner and Long* [2014a]

[a]Errors are two standard deviations of the background flow field and trench migration velocity estimates. α_s is the observed slab dip angle, D_{max} is the observed slab depth, and ϕ_s is the dominant seismic fast direction for each subduction zone taken from the indicated reference, where ∥ = trench-parallel and ⊥ = trench-perpendicular.

the coherent portion of the slab, which effectively acts as a shorter slab. Values for α and D_{max} can be found in Table 2.

We use the methods of [*Paczkowski et al.*, 2014] to estimate the regional mantle flow for each subduction zone from a global mantle circulation model [*Conrad and Behn*, 2010]. The global mantle circulation model is converted into a trench-fixed reference frame for each subduction zone by removing the average trench-perpendicular migration velocity [*Schellart et al.*, 2008] and the trench-parallel component of downgoing plate motion relative to the overriding plate [*DeMets et al.*, 1994]. The depth-averaged background mantle flow field is averaged along a transect where flow has been relatively unperturbed by the subduction zone, in a region that roughly corresponds to the back of our model. The online supplement presents the background velocity field for each subduction zone considered here and indicates the transect used for averaging. The resulting background mantle flow field is normalized by the trench-perpendicular component of the local convergence velocity, estimated as the difference between the trench-perpendicular velocities of the subducting plate and the overriding plate. The background flow velocity, $\bar{V}$, and azimuth, θ_v, for each subduction zone are reported in Table 2. Trench migration velocities and plate motion velocities are reported in supporting information Table S1.

4.4. Comparison Between Subslab Seismic Fast Directions and Model Results

All 25 subduction zones are grouped into five geometrical categories by rounding the slab dip to the nearest 15° and the slab depth to either 0.5 *D* (short slabs) or 1 *D* (long slabs). The general characterization of seismic anisotropy for each subduction zone segment is reported in Figure 8 as a function of background flow parameters for each category and compared with model predictions. We compare the subslab seismic anisotropy fast directions to the subslab mantle flow in fully decoupled models, with no lower mantle. As discussed in section 3, these assumptions do not greatly influence our results for background flow field and geometry of most subduction zones.

The majority of subduction zones in our data set have deep slabs, and the dip of 11 of these fall in the relatively steep 60° or 75° categories (Figures 8b and 8c). With the exception of Ryukyu, every subduction zone in this category displays dominantly trench-parallel fast splitting directions. Model results indicate

dominantly trench-parallel subslab mantle flow directions for nearly all background mantle flow cases with these slab geometries, in excellent agreement with anisotropy observations for these subduction zones. The background flow velocity in each of these cases is high enough that coupling up to $\mathcal{C} \approx 0.5$ at the base of the slab or including a lower mantle would not significantly affect these results (sections 3.3 and 3.4).

An additional nine subduction zones have deep slabs and slightly shallower dips, closer to $45°$ (Figure 8a). The anisotropy directions for these subduction zones show a mix of trench-parallel and trench-perpendicular fast splitting directions. Model results for this slab geometry are more strongly influenced by background mantle flow. The model predicts trench-parallel flow directions for subduction zone systems with trench-parallel background mantle flow, in agreement with observations in N. and S. South America, W. Sumatra, and C. Caribbean. Similarly, the model predicts more trench-perpendicular flow directions for systems with trench-perpendicular background mantle flow, such as Greece and Cascadia. However, our models do not match the observations for N. Honshu, and N. and S. Caribbean, which may reflect variations in coupling or the oversimplifications of our model, as discussed further below.

Finally, a number of subduction zones include short slabs that do not reach into the lower mantle (Figures 8d and 8e). In this case, it is possible for mantle to flow underneath the slab and the subslab mantle flow direction reflects the background mantle flow more directly than in the long slab cases, where this escape route is closed. As a result, trench-parallel subslab fast splitting directions are only predicted for a trench-parallel background flow field whereas trench-perpendicular flow is only expected in cases where background mantle flow is trench-perpendicular or the background flow velocity magnitude is very low. Consistent with these model predictions, the anisotropy observations for the subduction systems with a short slab geometry exhibit primarily trench-perpendicular fast directions, and the agreement between observations and our model predictions is generally good. Observations from Alaska, the Aleutians, Central America, and Mexico-Rivera match well with the predicted model results for the short geometry and trench-perpendicular background mantle flows.

5. Discussion

Previous studies have examined the possibility of three-dimensional flow in subduction zones. Laboratory models have documented three-dimensional mantle flow patterns, including toroidal flow, around a slab edge induced by trench migration [*Buttles and Olson*, 1998; *Kincaid and Griffiths*, 2003, 2004; *Funiciello et al.*, 2003, 2004, 2006; *Schellart*, 2004; *Druken et al.*, 2011]. However, most numerical studies have focused on the mantle wedge above the slab or on the slab edges [*Kneller and van Keken*, 2007, 2008; *Jadamec and Billen*, 2010, 2012]. *Faccenda and Capitanio* [2012, 2013] and *Li et al.* [2014] directly model the development of LPO fabric in the subslab mantle for a model setup similar to the laboratory models of *Buttles and Olson* [1998]. *Buttles and Olson* [1998], *Faccenda and Capitanio* [2012, 2013], *Di Leo et al.* [2014], and *Li et al.* [2014] found that three-dimensional flow is an important feature of subduction zone settings especially when trench migration (equivalent to the trench-fixed ambient background mantle flow field considered here), or regional slab morphology is included as part of the model setup. Synthetic SKS splitting orientations and delay times resulting from the numerical velocity field solutions are often consistent with those observed in naturally occurring subduction zones [*Miller and Becker*, 2012; *Faccenda and Capitanio*, 2012, 2013; *Di Leo et al.*, 2014; *Li et al.*, 2014], suggesting that numerical velocity fields provide a good approximation for the flow fields observed in natural settings.

Our work builds on these models by generating numerical velocity field solutions in the subslab mantle for a systematic variation of common subduction zone parameters. We find that three-dimensional subslab flow with a strong trench-parallel component is a robust result for all slab morphologies, boundary conditions, and a wide range of background mantle flow fields, particularly when the mechanical coupling between the slab and the subslab mantle is weak.

The abundance of subduction zone parameters and background mantle flow fields that produce three-dimensional subslab flow suggests that the interaction between background flow fields and the slab constitutes a reasonable explanation for the prevalence of trench-parallel fast splitting directions in the subslab mantle [*Long and Silver*, 2008, 2009]. However, our modeling work has shown that the relationships between flow directions and subduction zone parameters are often nonlinear, and isolating one parameter at a time will often result in inconclusive relationships. For example, in agreement with *Long and Silver*

[2008], a random sampling of subduction zones is unlikely to find any significant correlation between slab dip α and anisotropy azimuth ϕ as subduction zones with short slabs or fast trench-parallel background flow are insensitive to the slab dip angle. This may explain the generally poor correlations between subslab splitting delay times and many parameters that describe subduction [*Long and Silver*, 2009]. If there are similar nonlinear relationships between subduction parameters and mantle wedge flow fields, this may also explain the poor correlations among splitting parameters and subduction parameters in the mantle wedge as well [*Long and Wirth*, 2013].

Long and Silver [2008, 2009] noted a relationship between subslab delay times and trench migration velocity, suggesting that trench migration may induce strong, coherent, along-strike flow and result in strong trench-parallel subslab splitting. This hypothesis is generally borne out by our models, which explicitly include trench migration as part of the ambient background mantle flow. In a trench-fixed reference frame, a retreating trench migration velocity acts to increase the trench-perpendicular component of the background mantle flow field as the subducting slab rolls back through the subslab mantle. For most subduction zones, a retreating trench migration velocity acts to increase the magnitude $\bar{V}$ of the background mantle flow field, which may make the system less sensitive to other model parameters, such as slab dip, depth, and coupling, and which generally promotes three-dimensional flow in the subslab mantle. This may provide a first-order explanation for the trend in delay time with trench migration velocity denoted by *Long and Silver* [2008, 2009]; although the strength of anisotropy in the subslab mantle should scale with the amount of accumulated strain, not trench velocity per se [*Faccenda and Capitanio*, 2012, 2013], systems with rigid trench rollback are more likely to have accumulated a large amount of trench-parallel strain.

Our models represent a reasonable first step toward understanding the influence of slab geometry and background mantle flow on subslab velocity fields. However, they incorporate several simplifying assumptions. In particular, we use a rigid slab that does not evolve dynamically and we use a simple Newtonian viscosity. It is important to understand this simplified system before moving on to more complex systems; however, these assumptions and their possible influence on mantle flow warrant further discussion.

Our models consider the end-member scenario of a perfectly rigid slab. Subducted slabs are generally considered to have several hundred times higher viscosity than the surrounding mantle [*Billen et al.*, 2003; *Funiciello et al.*, 2008; *Schellart*, 2008; *Loiselet et al.*, 2009; *Schellart*, 2009; *Ribe*, 2010; *Stegman et al.*, 2010; *Li et al.*, 2014], suggesting that slabs are much less deformable than the surrounding mantle. However, observations [*Lallemand et al.*, 2005; *Syracuse and Abers*, 2006], experiments [*Schellart*, 2004] and geodynamic models [*Royden and Husson*, 2006; *Billen and Hirth*, 2007] show that slab dip and morphology are not constant over either the spatial extent of the subducting slab or the history of a subduction zone. The results presented here (section 3.4) as well as previous work [e.g., *King*, 2001; *Kneller and van Keken*, 2008; *Jadamec and Billen*, 2010; *Alisic et al.*, 2012] indicate that the flow field near subduction zones is sensitive to the changes in slab morphology and may result in spatial or temporal changes in the subslab flow field. The slab shape would likely respond to the pressure associated with the reorientation of flow that we observe in the subslab mantle [*Rodríguez-González et al.*, 2014b]. Therefore, a dynamic slab is likely to form less of an obstruction than we use here.

Perhaps the most uncertain parameter in our models is the amount of mechanical decoupling between the subducting plate and the subslab mantle. Model results depend greatly on the degree of coupling between the slab and the subslab mantle when the background mantle flow magnitude is low. Most seismic anisotropy observations, however, are from subduction zone segments where the background mantle flow magnitude, $\bar{V}$, is fast enough that we cannot evaluate reliably the degree of coupling. For subduction zone segments that have a low background mantle flow magnitude, the seismic anisotropy fast splitting directions are most consistent with at least partial decoupling between the slab and the subjacent mantle.

In our models, mechanical decoupling is accomplished by varying the coupling factor $\mathcal{C}$, but in natural systems, a physical mechanism is required. One possibility is that apparent decoupling between the subducting plate and the subslab mantle may arise from strain localization due to a non-Newtonian rheology. With a possible exception [*Miyazaki et al.*, 2013], the development of anisotropy in the upper mantle strongly suggests deformation is accommodated by dislocation creep [*Karato et al.*, 2008], which has a strong dependence on applied stresses [e.g., *Karato and Wu*, 1993; *Hirth and Kohlstedt*, 2004]. Other non-Newtonian rheologies may similarly localize deformation, including those that incorporate grain-size

sensitive reduction feedbacks [*Bercovici and Ricard*, 2012, 2014] or rheological anisotropy generated by LPO development [*Tommasi et al.*, 2009; *Lev and Hager*, 2011; *Hansen et al.*, 2012; *Montési*, 2013; *Skemer et al.*, 2013]. Non-Newtonian viscosities typically act to reduce the thickness of boundary layers relative to a Newtonian rheology, which may have the effect of thinning the subslab layer of entrained flow and act similarly to decoupling. Two-dimensional [*Parmentier et al.*, 1976; *Tovish et al.*, 1978; *McKenzie*, 1979] and three-dimensional [*Jadamec and Billen*, 2010, 2012; *Faccenda and Capitanio*, 2012, 2013] models using various non-Newtonian rheologies find that a spatially extensive viscosity reduction may arise in both the mantle wedge and the subslab mantle, the boundary layer entrained by the slab remains thicker than ≈ 100 km suggesting that an additional mechanism for decoupling may be required in order to be consistent with anisotropy observations. Additionally, other models have found no viscosity reduction in the subslab mantle [*Stadler et al.*, 2010b; *Alisic et al.*, 2012], further suggesting that an additional mechanism for decoupling may be required.

A number of conceptual models suggest that a thin, low-viscosity, decoupling layer may exist between the subducting plate and the subslab mantle. For example, *Phipps Morgan et al.* [2007], *Morgan et al.* [2013], and *Long and Silver* [2009] suggest $< \sim$ 30 km layer of low-viscosity asthenosphere may be entrained along with the subducting slab. This model requires a buoyant asthenosphere, which may indicate chemical depletion [*Phipps Morgan et al.*, 2007; *Morgan et al.*, 2013], shear heating [*Larsen et al.*, 1995; *Long and Silver*, 2009], high volatile content [*Karato and Jung*, 1998], or a minimum in water solubility of aluminous ortho-pyroxene [*Mierdel et al.*, 2007]. A second possible mechanism is the accumulation of partial melt along the interface between the subducting plate and the subslab mantle [e.g., *Green et al.*, 2010; *Hirschmann*, 2010; *Mierdel et al.*, 2007]. Such melts could cause the observed drop in vertically propagating shear wave velocities at the lithosphere-asthenosphere boundary (LAB) [*Backus*, 1962; *Rychert and Shearer*, 2009; *Kawakatsu et al.*, 2009] and act as a decoupling layer [*Holtzman et al.*, 2003; *Katz et al.*, 2006]. However, an usually high melt fraction is required to account for the observed seismic wave velocity drop and to create decoupling through grain-boundary wetting [*Karato*, 2012]. The melt fraction could be increased by migration [*Hebert and Montsi*, 2010] or the formation of a layered structure [*Kawakatsu et al.*, 2009], but the gravitational stability of such layering is questionable [*Hernlund et al.*, 2008a, 2008b].

Karato [2012] suggests that decoupling may result from a frozen gabbro melt layer directly beneath the LAB. In this model, the high water content of the transition zone [*Bercovici and Karato*, 2003; *Karato*, 2011] causes a large amount of partial melting of basaltic material to occur at 410 km. The negatively buoyant melt rises to 70 km depths and solidifies into a water-rich gabbro. The frozen melt accumulates over time, and for oceanic lithosphere as old as 100 Myr the layer should be ~0.1−1 km thick [*Karato*, 2012], small enough that it is not easily detected by seismic signals, but large enough to cause decoupling at the LAB. *Lynner and Long* [2014b] suggest a different mechanism for age-based decoupling, in which small-scale convection cells beneath old oceanic lithosphere may disrupt entrained flow beneath subducting slabs, and effectively act as a decoupling mechanism.

Regardless of the physical mechanism, the common observation of trench-parallel subslab fast splitting directions in the Earth's subduction zones [*Long and Silver*, 2008, 2009; *Lynner and Long*, 2014a] suggests at least partial decoupling between the subduction slab and the subslab mantle, if these observations are in fact due to three-dimensional subslab flow. Subduction zones with a fast trench-parallel background mantle flow (e.g., Calabria), however, are not likely to be affected by the degree of decoupling as our model would predict trench-parallel subslab flow directions even for a fully coupled subducting plate. Subduction zones with slow trench-parallel background flow (e.g., South America or W. Sumatra) are likely to be most sensitive to the amount of coupling. Our model does not distinguish among the various theories for decoupling between the subducting plate and the subslab mantle, but we suggest that detailed observations of seismic anisotropy combined with modeling have the potential to constrain the degree of coupling in real subduction zone systems.

Overall, the agreement between the observed seismic anisotropy directions and the fully decoupled model results is relatively favorable, though for several regions, (including Ryukyu, N. Honshu, and N. and S. Caribbean) the predictions and observations do not agree as well. We have investigated these correlations using a fully decoupled model (Figure 8), but as discussed above, different subduction zones may have different levels of decoupling, especially if the decoupling mechanism is age-dependent [*Karato*, 2012; *Lynner and Long*, 2014b] or depends on the specific geologic history of the subducting plate. A higher level of coupling in

subduction zones would increase the trench-perpendicular motion predicted by our model and better match the observed seismic anisotropy directions for Ryukyu, which subducts relatively young lithosphere (35–50 Ma) [*Heuret and Lallemand*, 2005]. The N. Honshu subduction zone contains a low magnitude, highly variable background mantle flow field (Table 2 and supporting information) and our average background mantle flow field may not accurately capture the ambient conditions for this subduction zone. Improved constraints on the background mantle flow may improve the correlation with our model results, especially if the regional flow is found to have an increased magnitude or a trench-parallel orientation. The N. and S. Caribbean subduction zone segments may contain additional constraints on deflection of mantle flow not captured by our model, including a close proximity the thick South American continental lithosphere [*Miller and Becker*, 2012; *Lynner and Long*, 2013] or a highly curved slab morphology. Finally, we mention that some authors have argued for fragmentation of the subducting slab in either the upper mantle [*Schmandt and Humphreys*, 2010; *Obrebski et al.*, 2011] or the transition zone [*Sigloch et al.*, 2008; *Roth et al.*, 2008; *Sigloch*, 2011; *James et al.*, 2011] in the Cascadia subduction zone. This fragmentation may allow the trench-perpendicular ambient background mantle flow to escape beneath the subducting plate and allow the slab to behave as a short slab. Shorter slabs tend to more closely reflect the ambient background mantle flow and allow for more trench-perpendicular subslab flow, which would agree with a Cascadia scenario.

As seismic anisotropy observations continue to be refined, additional discrepancies between the simplified models and observations may suggest behavior not captured by our model. For example, *Kneller and van Keken* [2007] and *Kneller et al.* [2008] find that slab morphology may create pressure-induced flow along the slab in the mantle wedge. The subslab mantle flow in the Caribbean subduction zone may be controlled by the highly curved morphology of the trench and slab, a parameter not included in our straight-trench model. The complex continental area at the southern end of the subduction zone may also affect mantle flow [*Lynner and Long*, 2013]. Slab width also likely influences the dynamics of the subduction zone systems [e.g., *Schellart et al.*, 2007], and subduction zones with very small slab widths may exhibit different subslab flow behavior. While our simplified model geometries provide a basis for understanding how different parameters (including slab geometries, kinematics, and boundary conditions) affect subslab flow, more realistic slab morphologies may influence the behavior of subslab mantle flow as well. Subduction zones that exhibit large discrepancies between seismic anisotropy observations and our model predictions are good candidates for focused study.

6. Summary

Our model experiments demonstrate that in general, three-dimensional flow in the subslab mantle occurs for nearly all subduction zone geometries, parameters, and boundary conditions, and is highly sensitive to the orientation and magnitude of the ambient background mantle flow. In general, the subducting slab acts as an obstruction to the ambient background mantle flow.

Whether the orientation of flow immediately beneath the subducting slab is dominantly trench-parallel or trench-perpendicular is highly sensitive to the orientation and magnitude of the background mantle flow field. Strong trench-parallel background flow continues through the subslab mantle largely unaffected by the presence of the subducting slab, especially when coupling is low. Trench-parallel background flow velocities with small magnitudes compete against the flow entrained by the subducting plate; for systems with relatively strong coupling, a boundary layer of two-dimensional entrained flow develops beneath the slab.

For cases in which the background velocity field is oriented perpendicular to the slab (e.g., corresponding to rapid trench rollback), the subducting slab acts as an obstruction to the background mantle flow. The background mantle flow may circumvent the obstructing slab by flowing either around the slab edges, creating dominantly trench-parallel subslab flow, or beneath the slab, creating dominantly trench-perpendicular subslab flow, depending on the slab geometry. Short slabs allow deflection beneath the slab, and as a result, the subslab flow in short slabs tends to reflect the orientation of the background mantle flow direction. In contrast, long slabs that penetrates to the lower mantle force background mantle flow along the back of the subducting slab toward slab edges, even when a high viscosity lower mantle is included in the model. Long slab systems are sensitive to the dip angle of the slab. Specifically, steeply dipping slabs efficiently deflect trench-perpendicular background mantle flow along the slab strike, creating dominantly trench-parallel subslab flow. More shallowly dipping slabs are less efficient at reorienting flow, and the resulting subslab flow directions demonstrate a mix of trench-parallel and trench-perpendicular flow directions, depending on the background mantle flow orientation and intensity.

We find that the subslab flow direction is not sensitive, or is only weakly sensitive, to other model parameters, including the presence and viscosity of the lower mantle or the character of the regional overriding plate (supporting information). In addition to slab geometry and background flow conditions, however, the model is highly sensitive to the amount of coupling between the subducting plate and the underlying subslab mantle. Coupling between the subducting plate and the subslab mantle generates a layer of trench-perpendicular entrained flow directly beneath the slab which can dominate the flow directions in the subslab mantle, especially for low magnitude background velocity flow fields.

We find a generally good correlation between the flow directions predicted by our model results and the first-order seismic anisotropy observations for a global data set of subduction zones evaluated in a trench-fixed reference frame. Subduction zones with long, steep slabs tend to exhibit primarily trench-parallel subslab fast splitting directions, while more shallow dip angles and shorter slabs tend to produce a mix of trench-parallel and trench-perpendicular fast directions, in general agreement with our model results. Discrepancies between predictions and observations in some individual subduction zones, however, suggest the possibility that in some regions additional factors such as slab curvature, slab width, or variations in subslab coupling may play a role in controlling mantle flow. If trench-parallel subslab fast splitting directions indeed reflect three-dimensional flow, our modeling suggests that mechanical coupling between slabs and the mantle beneath them may generally be weak, although this coupling may vary from region to region. While our models cannot rule out other explanations for trench-parallel fast splitting directions beneath slabs, [e.g., *Song and Kawakatsu*, 2012], they suggest that three-dimensional subslab flow represents a plausible geodynamic scenario for most subduction systems.

References

Alisic, L., M. Gurnis, G. Stadler, C. Burstedde, and O. Ghattas (2012), Multi-scale dynamics and rheology of mantle flow with plates, *J. Geophys. Res.*, *117*, B10402, doi:10.1029/2012JB009234.

Anderson, M. L., G. Zandt, E. Triep, M. Fouch, and S. Beck (2004), Anisotropy and mantle flow in the Chile-Argentina subduction zone from shear wave splitting analysis, *Geophys. Res. Lett.*, *31*, L23608, doi:10.1029/2004GL020906.

Baccheschi, P., L. Margheriti, and M. Steckler (2008), SKS splitting in Southern Italy: Anisotropy variations in a fragmented subduction zone, *Tectonophysics*, *462*(14), 49–67, doi:10.1016/j.tecto.2007.10.014.

Baccheschi, P., L. Margheriti, M. S. Steckler, and E. Boschi (2011), Anisotropy patterns in the subducting lithosphere and in the mantle wedge: A case study the southern Italy subduction system, *J. Geophys. Res.*, *116*, B08306, doi:10.1029/2010JB007961.

Backus, G. E. (1962), Long-wave elastic anisotropy produced by horizontal layering, *J. Geophys. Res.*, *67*(11), 4427–4440, doi:10.1029/JZ067i011p04427.

Becker, T. W. (2008), Azimuthal seismic anisotropy constrains net rotation of the lithosphere, *Geophys. Res. Lett.*, *35*, L05303, doi:10.1029/2007GL032928.

Bercovici, D., and S.-I. Karato (2003), Whole-mantle convection and the transition-zone water filter, *Nature*, *425*(6953), 39–44, doi:10.1038/nature01918.

Bercovici, D., and Y. Ricard (2012), Mechanisms for the generation of plate tectonics by two-phase grain-damage and pinning, *Phys. Earth Planet. Inter.*, *202–203*, 27–55, doi:10.1016/j.pepi.2012.05.003.

Bercovici, D., and Y. Ricard (2014), Plate tectonics, damage and inheritance, *Nature*, *508*, 513–516, doi:10.1038/nature13072.

Billen, M. I., and G. Hirth (2007), Rheologic controls on slab dynamics, *Geochem. Geophys. Geosyst.*, *8*, Q08012, doi:10.1029/2007GC001597.

Billen, M. I., M. Gurnis, and M. Simons (2003), Multiscale dynamics of the Tonga-Kermadec subduction zone, *Geophys. J. Int.*, *153*(2), 359–388, doi:10.1046/j.1365-246X.2003.01915.x.

Bostock, M. G., and J. C. Vandecar (1995), Upper mantle structure of the northern Cascadia subduction zone, *Can. J. Earth Sci.*, *32*(1), 1–12, doi:10.1139/e95-001.

Buttles, J., and P. Olson (1998), A laboratory model of subduction zone anisotropy, *Earth Planet. Sci. Lett.*, *164*(1–2), 245–262, doi:10.1016/S0012-821X(98)00211-8.

Conrad, C. P., and M. D. Behn (2010), Constraints on lithosphere net rotation and asthenospheric viscosity from global mantle flow models and seismic anisotropy, *Geochem. Geophys. Geosyst.*, *11*, Q05W05, doi:10.1029/2009GC002970.

DeMets, C., R. G. Gordon, D. F. Argus, and S. Stein (1994), Effect of recent revisions to the geomagnetic reversal time scale on estimates of current plate motions, *Geophys. Res. Lett.*, *21*, 2191–2194.

Di Leo, J. F., A. M. Walker, Z.-H. Li, J. Wookey, N. M. Ribe, J.-M. Kendall, and A. Tommasi (2014), Development of texture and seismic anisotropy during the onset of subduction, *Geochem. Geophys. Geosyst.*, *15*, 192–212, doi:10.1002/2013GC005032.

Druken, K. A., M. D. Long, and C. Kincaid (2011), Patterns in seismic anisotropy driven by rollback subduction beneath the high lava plains, *Geophys. Res. Lett.*, *38*, L13310, doi:10.1029/2011GL047541.

Eakin, C. M., M. Obrebski, R. M. Allen, D. C. Boyarko, M. R. Brudzinski, and R. Porritt (2010), Seismic anisotropy beneath Cascadia and the Mendocino triple junction: Interaction of the subducting slab with mantle flow, *Earth Planet. Sci. Lett.*, *297*(3–4), 627–632, doi:10.1016/j.epsl.2010.07.015.

Faccenda, M., and F. A. Capitanio (2012), Development of mantle seismic anisotropy during subduction-induced 3-D flow, *Geophys. Res. Lett.*, *39*, L11305, doi:10.1029/2012GL051988.

Faccenda, M., and F. A. Capitanio (2013), Seismic anisotropy around subduction zones: Insights from three-dimensional modeling of upper mantle deformation and SKS splitting calculations, *Geochem. Geophys. Geosyst.*, *14*, 243–262, doi:10.1002/ggge.20055.

Faccenda, M., L. Burlini, T. Gerya, and D. Mainprice (2008), Fault-induced seismic anisotropy by hydration in subducting oceanic plates, *Nature*, *455*, 1097–1100, doi:10.1038/nature07376.

Fischer, K. M., E. M. Parmentier, A. R. Stine, and E. R. Wolf (2000), Modeling anisotropy and plate-driven flow in the Tonga subduction zone back arc, *J. Geophys. Res.*, *105*(B7), 16,181–16,191, doi:10.1029/1999JB900441.

Foley, B. J., and M. D. Long (2011), Upper and mid-mantle anisotropy beneath the Tonga slab, *Geophys. Res. Lett.*, *38*, L02303, doi:10.1029/2010GL046021.

Funiciello, F., C. Faccenna, D. Giardini, and K. Regenauer-Lieb (2003), Dynamics of retreating slabs. 2: Insights from three-dimensional laboratory experiments, *J. Geophys. Res.*, *108*(B4), 2207, doi:10.1029/2001JB000896.

Funiciello, F., C. Faccenna, and D. Giardini (2004), Role of lateral mantle flow in the evolution of subduction systems: Insights from laboratory experiments, *Geophys. J. Int.*, *157*(3), 1393–1406, doi:10.1111/j.1365-246X.2004.02313.x.

Funiciello, F., M. Moroni, C. Piromallo, C. Faccenna, A. Cenedese, and H. A. Bui (2006), Mapping mantle flow during retreating subduction: Laboratory models analyzed by feature tracking, *J. Geophys. Res.*, *111*, B03402, doi:10.1029/2005JB003792.

Funiciello, F., C. Faccenna, A. Heuret, S. Lallemand, E. Di Giuseppe, and T. W. Becker (2008), Trench migration, net rotation and slab mantle coupling, *Earth Planet. Sci. Lett.*, *271*, 233–240, doi:10.1016/j.epsl.2008.04.006.

Green, D., W. Hibberson, I. Kovács, and A. Rosenthal (2010), Water and its influence on the lithosphere-asthenosphere boundary, *Nature*, *467*, 448–452, doi:10.1038/nature09369.

Hammond, J., J. Wookey, S. Kaneshima, H. Inoue, T. Yamashina, and P. Harjadi (2010), Systematic variation in anisotropy beneath the mantle wedge in the Java–Sumatra subduction system from shear-wave splitting, *Phys. Earth Planet. Inter.*, *178*(3–4), 189–201, doi:10.1016/j.pepi.2009.10.003.

Hanna, J., and M. D. Long (2012), SKS splitting beneath Alaska: Regional variability and implications for subduction processes at a slab edge, *Tectonophysics*, *530–531*, 272–285, doi:10.1016/j.tecto.2012.01.003.

Hanna, J., M. Long, and M. Brudzinski (2009), Distinguishing wedge, slab, and sub-slab anisotropy in the Izu-Bonin-Mariana subduction zone, *Eos Trans. AGU*, *90*(52), Fall Meet. Suppl., Abstract B1803.

Hansen, L., M. Zimmerman, and D. Kohlstedt (2012), Laboratory measurements of the viscous anisotropy of olivine aggregates, *Nature*, *492*(7429), 415–418, doi:10.1038/nature11671.

Hebert, L. B., and L. G. J. Montsi (2010), Generation of permeability barriers during melt extraction at mid-ocean ridges, *Geochem. Geophys. Geosyst.*, *11*, Q12008, doi:10.1029/2010GC003270.

Hernlund, J. W., D. J. Stevenson, and P. J. Tackley (2008a), Buoyant melting instabilities beneath extending lithosphere. 2: Linear analysis, *J. Geophys. Res.*, *113*, B04406, doi:10.1029/2006JB004863.

Hernlund, J. W., P. J. Tackley, and D. J. Stevenson (2008b), Buoyant melting instabilities beneath extending lithosphere. 1: Numerical models, *J. Geophys. Res.*, *113*, B04405, doi:10.1029/2006JB004862.

Heuret, A., and S. Lallemand (2005), Plate motions, slab dynamics and back-arc deformation, *Phys. Earth Planet. Inter.*, *149*(1–2), 31–51, doi:10.1016/j.pepi.2004.08.022.

Hirschmann, M. M. (2010), Partial melt in the oceanic low velocity zone, *Phys. Earth Planet. Inter.*, *179*(1–2), 60–71, doi:10.1016/j.pepi.2009.12.003.

Hirth, G., and D. Kohlstedt (2004), Rheology of the upper mantle and the mantle wedge: A view from the experimentalists, in *Inside the Subduction Factory*, edited by J. Eiler, pp. 83–105, AGU, Washington, D. C., doi:10.1029/138GM06.

Holtzman, B. K., D. L. Kohlstedt, M. E. Zimmerman, F. Heidelbach, T. Hiraga, and J. Hustoft (2003), Melt segregation and strain partitioning: Implications for seismic anisotropy and mantle flow, *Science*, *301*(5637), 1227–1230, doi:10.1126/science.1087132.

Jadamec, M., and M. Billen (2010), Reconciling surface plate motion and rapid three-dimensional flow around a slab edge, *Nature*, *465*, 338–342, doi:10.1038/nature09053.

Jadamec, M. A., and M. I. Billen (2012), The role of rheology and slab shape on rapid mantle flow: Three-dimensional numerical models of the Alaska slab edge, *J. Geophys. Res.*, *117*, B02304, doi:10.1029/2011JB008563.

James, D. E., M. J. Fouch, R. W. Carlson, and J. B. Roth (2011), Slab fragmentation, edge flow and the origin of the yellowstone hotspot track, *Earth Planet. Sci. Lett.*, *311*(1–2), 124–135, doi:10.1016/j.epsl.2011.09.007.

Jarrard, R. D. (1986), Relations among subduction parameters, *Rev. Geophys.*, *24*(2), 217–284, doi:10.1029/RG024i002p00217.

Jung, H., and S.-I. Karato (2001), Water-induced fabric transitions in olivine, *Science*, *293*(5534), 1460–1463, doi:10.1126/science.1062235.

Jung, H., I. Katayama, Z. Jiang, T. Hiraga, and S. Karato (2006), Effect of water and stress on the lattice-preferred orientation of olivine, *Tectonophysics*, *421*(1–2), 1–22, doi:10.1016/j.tecto.2006.02.011.

Jung, H., W. Mo, and W. Green (2009), Upper mantle seismic anisotropy resulting from pressure-induced slip transition in olivine, *Nat. Geosci.*, *2*, 73–77, doi:10.1038/ngeo389.

Kaminski, E., N. Ribe, and J. Browaeys (2004), D-Rex, a program for calculation of seismic anisotropy due to crystal lattice preferred orientation in the convective upper mantle, *Geophys. J. Int.*, *158*(2), 744–752, doi:10.1111/j.1365-246X.2004.02308.x.

Karato, S.-I. (2011), Some issues on the strength of the lithosphere, *J. Earth Sci.*, *22*(2), 131–136, doi:10.1007/s12583-011-0164-y.

Karato, S.-I. (2012), On the origin of the asthenosphere, *Earth Planet. Sci. Lett.*, *321–322*, 95–103, doi:10.1016/j.epsl.2012.01.001.

Karato, S.-I., and H. Jung (1998), Water, partial melting and the origin of the seismic low velocity and high attenuation zone in the upper mantle, *Earth Planet. Sci. Lett.*, *157*(3–4), 193–207, doi:10.1016/S0012-821X(98)00034-X.

Karato, S.-I., and P. Wu (1993), Rheology of the upper mantle: A synthesis, *Science*, *260*(5109), 771–778, doi:10.1126/science.260.5109.771.

Karato, S.-I., H. Jung, I. Katayama, and P. Skemer (2008), Geodynamic significance of seismic anisotropy of the upper mantle: New insights from laboratory studies, *Annu. Rev. Earth Planet. Sci.*, *36*, 59–95, doi:10.1146/annurev.earth.36.031207.124120.

Katayama, I., and S.-I. Karato (2006), Effect of temperature on the B- to C-type olivine fabric transition and implication for flow pattern in subduction zones, *Phys. Earth Planet. Inter.*, *157*(1–2), 33–45, doi:10.1016/j.pepi.2006.03.005.

Katayama, I., H. Jung, and S.-I. Karato (2004), New type of olivine fabric from deformation experiments at modest water content and low stress, *Geology*, *32*(12), 1045–1048, doi:10.1130/G20805.1.

Katz, R., M. Spiegelman, and B. Holtzman (2006), The dynamics of melt and shear localization in partially molten aggregates, *Nature*, *442*, 676–679, doi:10.1038/nature05039.

Kawakatsu, H., P. Kumar, Y. Takei, M. Shinohara, T. Kanazawa, E. Araki, and K. Suyehiro (2009), Seismic evidence for sharp lithosphere-asthenosphere boundaries of oceanic plates, *Science*, *324*(5926), 499–502, doi:10.1126/science.1169499.

Kincaid, C., and R. Griffiths (2003), Laboratory models of the thermal evolution of the mantle during rollback subduction, *Nature*, *425*, 58–62, doi:10.1038/nature01923.

Kincaid, C., and R. W. Griffiths (2004), Variability in flow and temperatures within mantle subduction zones, *Geochem. Geophys. Geosyst.*, *5*, Q06002, doi:10.1029/2003GC000666.

King, S. D. (2001), Subduction zones: Observations and geodynamic models, *Phys. Earth Planet. Inter.*, *127*, 9–24, doi:10.1016/S0031-9201(01)00218-7.

Király, E., I. Bianchi, and G. Bokelmann (2012), Seismic anisotropy in the south western Pacific region from shear wave splitting, *Geophys. Res. Lett.*, *39*, L05302, doi:10.1029/2011GL050407.

Kneller, E., and P. van Keken (2007), Trench-parallel flow and seismic anisotropy in the Mariana and Andean subduction systems, *Nature*, *450*, 1222–1226, doi:10.1038/nature06429.

Kneller, E., and P. van Keken (2008), Effect of three-dimensional slab geometry on deformation in the mantle wedge: Implications for shear wave anisotropy, *Geochem. Geophys. Geosyst.*, *9*, Q01003, doi:10.1029/2007GC001677.

Kneller, E. A., P. E. van Keken, S.-I. Karato, and J. Park (2005), B-type olivine fabric in the mantle wedge: Insights from high-resolution non-Newtonian subduction zone models, *Earth Planet. Sci. Lett.*, *237*(3–4), 781–797, doi:10.1016/j.epsl.2005.06.049.

Kneller, E. A., M. D. Long, and P. E. van Keken (2008), Olivine fabric transitions and shear wave anisotropy in the Ryukyu subduction system, *Earth Planet. Sci. Lett.*, *268*(3–4), 268–282, doi:10.1016/j.epsl.2008.01.004.

Kreemer, C. (2009), Absolute plate motions constrained by shear wave splitting orientations with implications for hot spot motions and mantle flow, *J. Geophys. Res.*, *114*, B10405, doi:10.1029/2009JB006416.

Lallemand, S., A. Heuret, and D. Boutelier (2005), On the relationships between slab dip, back-arc stress, upper plate absolute motion, and crustal nature in subduction zones, *Geochem. Geophys. Geosyst.*, *6*, Q09006, doi:10.1029/2005GC000917.

Larsen, T. B., D. A. Yuen, and A. V. Malevsky (1995), Dynamical consequences on fast subducting slabs from a self-regulating mechanism due to viscous heating in variable viscosity convection, *Geophys. Res. Lett.*, *22*(10), 1277–1280, doi:10.1029/95GL01112.

León Soto, J., J. Ni, S. Grand, E. Sandvol, R. Valenzuela, M. G. Speziale, J. G. González, and T. D. Reyes (2009), Mantle flow in the Rivera-Cocos subduction zone, *Geophys. J. Int.*, *179*, 1004–1012, doi:10.1111/j.1365-246X.2009.04352.x.

Lev, E., and B. H. Hager (2011), Anisotropic viscosity changes subduction zone thermal structure, *Geochem. Geophys. Geosyst.*, *12*, Q04009, doi:10.1029/2010GC003382.

Li, Z.-H., J. F. Di Leo, and N. M. Ribe (2014), Subduction-induced mantle flow, finite strain, and seismic anisotropy: Numerical modeling, *J. Geophys. Res.*, *119*, 5052–5076, doi:10.1002/2014JB010996.

Loiselet, C., L. Husson, and J. Braun (2009), From longitudinal slab curvature to slab rheology, *Geology*, *37*(8), 747–750, doi:10.1130/G30052A.1.

Long, M., B. Hager, M. de Hoop, and R. van der Hilst (2007), Two-dimensional modeling of subduction zone anisotropy with application to southwest Japan, *Geophys. J. Int.*, *170*(2), 839–856, doi:10.1111/j.1365-246X.2007.03464.x.

Long, M. D. (2013), Constraints on subduction geodynamics from seismic anisotropy, *Rev. Geophys.*, *51*, 76–112, doi:10.1002/rog.20008.

Long, M. D., and T. W. Becker (2010), Mantle dynamics and seismic anisotropy, *Earth Planet. Sci. Lett.*, *297*(3–4), 341–354, doi:10.1016/j.epsl.2010.06.036.

Long, M. D., and P. G. Silver (2008), The subduction zone flow field from seismic anisotropy: A global view, *Science*, *319*(5861), 315–318, doi:10.1126/science.1150809.

Long, M. D., and P. G. Silver (2009), Mantle flow in subduction systems: The subslab flow field and implications for mantle dynamics, *J. Geophys. Res.*, *114*, B10312, doi:10.1029/2008JB006200.

Long, M. D., and E. A. Wirth (2013), Mantle flow in subduction systems: The mantle wedge flow field and implications for wedge processes, *J. Geophys. Res.*, *118*, 583–606, doi:10.1002/jgrb.50063.

Lowman, J. P., L. T. Pinero-Feliciangeli, J.-M. Kendall, and M. H. Shahnas (2007), Influence of convergent plate boundaries on upper mantle flow and implications for seismic anisotropy, *Geochem. Geophys. Geosyst.*, *8*, Q08007, doi:10.1029/2007GC001627.

Lynner, C., and M. D. Long (2013), Sub-slab seismic anisotropy and mantle flow beneath the Caribbean and Scotia subduction zones: Effects of slab morphology and kinematics, *Earth Planet. Sci. Lett.*, *361*, 367–378, doi:10.1016/j.epsl.2012.11.007.

Lynner, C., and M. D. Long (2014a), Sub-slab anisotropy beneath the Sumatra and circum-Pacific subduction zones from source-side shear wave splitting observations, *Geochem. Geophys. Geosyst.*, *15*, 2262–2281, doi:10.1002/2014GC005239.

Lynner, C., and M. D. Long (2014b), Testing models of sub-slab anisotropy using a global compilation of source-side shear wave splitting data, *J. Geophys. Res. Solid Earth*, *119*, 7226–7244, doi:10.1002/2014JB010983.

Mainprice, D. (2007), Seismic anisotropy of the deep earth from a mineral and rock physics perspective, in *Treatise on Geophysics*, edited by G. Schubert, pp. 437–491, Elsevier, Amsterdam, doi:10.1016/B978-044452748-6.00045-6.

McKenzie, D. (1979), Finite deformation during fluid flow, *Geophys. J. R. Astron. Soc.*, *58*(3), 689–715, doi:10.1111/j.1365-246X.1979.tb04803.x.

Mierdel, K., H. Keppler, J. R. Smyth, and F. Langenhorst (2007), Water solubility in aluminous orthopyroxene and the origin of earth's asthenosphere, *Science*, *315*(5810), 364–368, doi:10.1126/science.1135422.

Miller, M. S., and T. W. Becker (2012), Mantle flow deflected by interactions between subducted slabs and Cratonic keels, *Nat. Geosci.*, *5*(10), 726–730, doi:10.1038/ngeo1553.

Miyazaki, T., K. Sueyoshi, and T. Hiraga (2013), Olivine crystals align during diffusion creep of Earth's upper mantle, *Nature*, *502*(7471), 321–326, doi:10.1038/nature12570.

Montési, L. G. (2013), Fabric development as the key for forming ductile shear zones and enabling plate tectonics, *J. Struct. Geol.*, *50*, 254–266, doi:10.1016/j.jsg.2012.12.011.

Morgan, J., J. Hasenclever, and C. Shi (2013), New observational and experimental evidence for a plume-fed asthenosphere boundary layer in mantle convection, *Earth Planet. Sci. Lett.*, *366*, 99–111, doi:10.1016/j.epsl.2013.02.001.

Morgan, W. J. (1968), Rises, trenches, great faults, and crustal blocks, *J. Geophys. Res.*, *73*(6), 1959–1982, doi:10.1029/JB073i006p01959.

Müller, C., B. Bayer, A. Eckstaller, and H. Miller (2008), Mantle flow in the South Sandwich subduction environment from source-side shear wave splitting, *Geophys. Res. Lett.*, *35*, L03301, doi:10.1029/2007GL032411.

Obrebski, M., R. M. Allen, F. Pollitz, and S.-H. Hung (2011), Lithosphere–asthenosphere interaction beneath the western United States from the joint inversion of body-wave traveltimes and surface-wave phase velocities, *Geophys. J. Int.*, *185*(2), 1003–1021, doi:10.1111/j.1365-246X.2011.04990.x.

Olive, J.-A., F. Pearce, S. Rondenay, and M. D. Behn (2014), Pronounced zonation of seismic anisotropy in the Western Hellenic subduction zone and its geodynamic significance, *Earth Planet. Sci. Lett.*, *391*, 100–109, doi:10.1016/j.epsl.2014.01.029.

Paczkowski, K., C. J. Thissen, M. D. Long, and L. G. J. Montési (2014), Deflection of mantle flow beneath subducting slabs and the origin of sub-slab anistropy, *Geophys. Res. Lett.*, *41*, doi:10.1002/2014GL060914, in press.

Parmentier, E. M., D. L. Turcotte, and K. E. Torrance (1976), Studies of finite amplitude non-Newtonian thermal convection with application to convection in the earth's mantle, *J. Geophys. Res.*, *81*(11), 1839–1846, doi:10.1029/JB081i011p01839.

Peyton, V., V. Levin, J. Park, M. Brandon, J. Lees, E. Gordeev, and A. Ozerov (2001), Mantle flow at a slab edge: Seismic anisotropy in the Kamchatka Region, *Geophys. Res. Lett.*, *28*(2), 379–382, doi:10.1029/2000GL012200.

Phipps Morgan, J., J. Hasenclever, M. Hort, L. Rüpke, and E. M. Parmentier (2007), On subducting slab entrainment of buoyant asthenosphere, *Terra Nova*, *19*(3), 167–173, doi:10.1111/j.1365-3121.2007.00737.x.

Ribe, N. M. (1989), A continuum theory for lattice preferred orientation, *Geophys. J. Int.*, *97*(2), 199–207, doi:10.1111/j.1365-246X.1989.tb00496.x.

Ribe, N. M. (1992), On the relation between seismic anisotropy and finite strain, *J. Geophys. Res.*, *97*(B6), 8737–8747, doi:10.1029/92JB00551.

Ribe, N. M. (2010), Bending mechanics and mode selection in free subduction: A thin-sheet analysis, *Geophys. J. Int.*, *180*(2), 559–576, doi:10.1111/j.1365-246X.2009.04460.x.

Rodríguez-González, J., M. I. Billen, and A. M. Negredo (2014a), Non-steady-state subduction and trench-parallel flow induced by overriding plate structure, *Earth Planet. Sci. Lett.*, *401*, 227–235.

Rodríguez-González, J., A. M. Negredo, and E. Carminati (2014b), Slab-mantle flow interaction: Influence on subduction dynamics and duration, *Terra Nova*, *26*(4), 265–272, doi:10.1111/ter.12095.

Roth, J. B., M. J. Fouch, D. E. James, and R. W. Carlson (2008), Three-dimensional seismic velocity structure of the northwestern United States, *Geophys. Res. Lett.*, *35*, L15304, doi:10.1029/2008GL034669.

Royden, L. H., and L. Husson (2006), Trench motion, slab geometry and viscous stresses in subduction systems, *Geophys. J. Int.*, *167*(2), 881–905, doi:10.1111/j.1365-246X.2006.03079.x.

Russo, R. (2009), Subducted oceanic asthenosphere and upper mantle flow beneath the Juan de Fuca slab, *Lithosphere*, *1*(4), 195–205, doi:10.1130/L41.1.

Russo, R. M., and P. G. Silver (1994), Trench-parallel flow beneath the Nazca plate from seismic anisotropy, *Science*, *263*(5150), 1105–1111, doi:10.1126/science.263.5150.1105.

Rychert, C. A., and P. M. Shearer (2009), A global view of the lithosphere-asthenosphere boundary, *Science*, *324*(5926), 495–498, doi:10.1126/science.1169754.

Savage, M. K. (1999), Seismic anisotropy and mantle deformation: What have we learned from shear wave splitting?, *Rev. Geophys.*, *37*(1), 65–106, doi:10.1029/98RG02075.

Schellart, W. P. (2004), Kinematics of subduction and subduction-induced flow in the upper mantle, *J. Geophys. Res.*, *109*, B07401, doi:10.1029/2004JB002970.

Schellart, W. P. (2008), Kinematics and flow patterns in deep mantle and upper mantle subduction models: Influence of the mantle depth and slab to mantle viscosity ratio, *Geochem. Geophys. Geosyst.*, *9*, Q03014, doi:10.1029/2007GC001656.

Schellart, W. P. (2009), Evolution of the slab bending radius and the bending dissipation in three-dimensional subduction models with a variable slab to upper mantle viscosity ratio, *Earth Planet. Sci. Lett.*, *288*(1–2), 309–319, doi:10.1016/j.epsl.2009.09.034.

Schellart, W. P., J. Freeman, D. Stegman, L. Moresi, and D. May (2007), Evolution and diversity of subduction zones controlled by slab width, *Nature*, *446*(7133), 308–311, doi:10.1038/nature05615.

Schellart, W. P., D. Stegman, and J. Freeman (2008), Global trench migration velocities and slab migration induced upper mantle volume fluxes: Constraints to find an Earth reference frame based on minimizing viscous dissipation, *Earth Sci. Rev.*, *88*(1–2), 118–144, doi:10.1016/j.earscirev.2008.01.005.

Schmandt, B., and E. Humphreys (2010), Complex subduction and small-scale convection revealed by body-wave tomography of the western United States upper mantle, *Earth Planet. Sci. Lett.*, *297*(3–4), 435–445, doi:10.1016/j.epsl.2010.06.047.

Sigloch, K. (2011), Mantle provinces under North America from multifrequency P wave tomography, *Geochem. Geophys. Geosyst.*, *12*, Q02W08, doi:10.1029/2010GC003421.

Sigloch, K., N. McQuarrie, and G. Nolet (2008), Two-stage subduction history under North America inferred from multiple-frequency tomography, *Nat. Geosci.*, *1*(7), 458–462, doi:10.1038/ngeo231.

Skemer, P., J. M. Warren, and G. Hirth (2012), The influence of deformation history on the interpretation of seismic anisotropy, *Geochem. Geophys. Geosyst.*, *13*, Q03006, doi:10.1029/2011GC003988.

Skemer, P., J. M. Warren, L. N. Hansen, G. Hirth, and P. B. Kelemen (2013), The influence of water and LPO on the initiation and evolution of mantle shear zones, *Earth Planet. Sci. Lett.*, *375*, 222–233, doi:10.1016/j.epsl.2013.05.034.

Song, T.-R. A., and H. Kawakatsu (2012), Subduction of oceanic asthenosphere: Evidence from sub-slab seismic anisotropy, *Geophys. Res. Lett.*, *39*, L17301, doi:10.1029/2012GL052639.

Song, T.-R. A., and H. Kawakatsu (2013), Subduction of oceanic asthenosphere: A critical appraisal in central Alaska, *Earth Planet. Sci. Lett.*, *367*, 82–94, doi:10.1016/j.epsl.2013.02.010.

Stadler, G., M. Gurnis, C. Burstedde, L. C. Wilcox, L. Alisic, and O. Ghattas (2010a), The dynamics of plate tectonics and mantle flow: From local to global scales, *Science*, *329*(5995), 1033–1038, doi:10.1126/science.1191223.

Stadler, G., M. Gurnis, C. Burstedde, L. Wilcox, L. Alisic, and O. Ghattas (2010b), The dynamics of plate tectonics and mantle flow: From local to global scales, *Science*, *329*(5995), 1033–1038, doi:10.1126/science.1191223.

Stegman, D., R. Farrington, F. Capitanio, and W. Schellart (2010), A regime diagram for subduction styles from 3-D numerical models of free subduction, *Tectonophysics*, *483*(1–2), 29–45, doi:10.1016/j.tecto.2009.08.041.

Suckale, J., S. Rondenay, M. Sachpazi, M. Charalampakis, A. Hosa, and L. H. Royden (2009), High-resolution seismic imaging of the western Hellenic subduction zone using teleseismic scattered waves, *Geophys. J. Int.*, *178*(2), 775–791, doi:10.1111/j.1365-246X.2009.04170.x.

Syracuse, E. M., and G. A. Abers (2006), Global compilation of variations in slab depth beneath arc volcanoes and implications, *Geochem. Geophys. Geosyst.*, *7*, Q05017, doi:10.1029/2005GC001045.

Tommasi, A., D. Mainprice, G. Canova, and Y. Chastel (2000), Viscoplastic self-consistent and equilibrium-based modeling of upper mantle seismic anisotropy, *J. Geophys. Res.*, *105*(B4), 7893–7908, doi:10.1029/1999JB900411.

Tommasi, A., M. Knoll, A. Vauchez, J. W. Signorelli, C. Thoraval, and R. Logé (2009), Structural reactivation in plate tectonics controlled by olivine crystal anisotropy, *Nat. Geosci.*, *2*(6), 423–427, doi:10.1038/ngeo528.

Tovish, A., G. Schubert, and B. P. Luyendyk (1978), Mantle flow pressure and the angle of subduction: Non-Newtonian corner flows, *J. Geophys. Res.*, *83*(B12), 5892–5898, doi:10.1029/JB083iB12p05892.

van Keken, P. E. et al. (2008), A community benchmark for subduction zone modeling, *Phys. Earth Planet. Inter.*, *171*(1–4), 187–197, doi:10.1016/j.pepi.2008.04.015.

Wada, I., and K. Wang (2009), Common depth of slab-mantle decoupling: Reconciling diversity and uniformity of subduction zones, *Geochem. Geophys. Geosyst.*, *10*, Q10009, doi:10.1029/2009GC002570.

Wookey, J., J.-M. Kendall, and G. Rümpker (2005), Lowermost mantle anisotropy beneath the north pacific from differential S-ScS splitting, *Geophys. J. Int.*, *161*(3), 829–838, doi:10.1111/j.1365-246X.2005.02623.x.